

Role of spatial inhomogeneity in dissociation of trapped molecular condensates

Magnus Ögren and K. V. Kheruntsyan

*ARC Centre of Excellence for Quantum-Atom Optics, School of Mathematics and Physics,
University of Queensland, Brisbane, Queensland 4072, Australia*

(Received 4 May 2009; revised manuscript received 25 May 2010; published 28 July 2010)

We theoretically analyze dissociation of a harmonically trapped Bose-Einstein condensate of molecular dimers and examine how the spatial inhomogeneity of the molecular condensate affects the conversion dynamics and the atom-atom pair correlations in the short-time limit. Both fermionic and bosonic statistics of the constituent atoms are considered. Using the undepleted molecular-field approximation, we obtain explicit analytic results for the asymptotic behavior of the second-order correlation functions and for the relative number squeezing between the dissociated atoms in one, two, and three spatial dimensions. Comparison with the numerical results shows that the analytic approach employed here captures the main underlying physics and provides useful insights into the dynamics of dissociation for conversion efficiencies up to 10%. The results show explicitly how the strength of atom-atom correlations and relative number squeezing degrade with the reduction of the size of the molecular condensate.

DOI: [10.1103/PhysRevA.82.013641](https://doi.org/10.1103/PhysRevA.82.013641)

PACS number(s): 03.75.-b, 03.65.-w, 05.30.-d, 33.80.Gj

I. INTRODUCTION

Pair production of photons has been the key mechanism in a series of landmark experiments in quantum optics. Of particular importance have been the experiments with pair correlated photons from an atomic radiative cascade [1] and from parametric down-conversion [2,3], leading to demonstrations of violations of Bell's inequalities and the Einstein-Podolsky-Rosen (EPR) entanglement [4–7]. Performed initially with *discrete* polarization states of photons—as a realization of Bohm's version [8] of the EPR gedankenexperiment [9]—the EPR correlations have been later demonstrated in their original version, that is, for a system of observables with a *continuous* spectrum [10]. In this case, the role of a pair of canonically conjugate variables is taken by quadrature amplitudes of spatially separated signal and idler beams generated using a nondegenerate parametric down-conversion in a cavity.

In atom optics, one of the simplest mechanisms for atom pair production can be realized via dissociation of diatomic molecules [11–15]. When performed using a molecular Bose-Einstein condensate (BEC) as the initial state and assuming that the constituent atoms are bosons, the process lends itself [16–19] as a direct matter-wave analog of optical parametric down-conversion of an intense laser light in a $\chi^{(2)}$ -nonlinear crystal. Owing to this analogy, one can envisage that future experiments on dissociation of molecular BECs can lead to atom optics demonstrations of EPR correlations [20–22] and related tests of Bell's inequalities [23,24].

The most important ingredients for such experiments are (i) the creation of quantum degenerate samples of stable, long-lived molecules, preferably in a rovibrational ground state (such as in recently demonstrated experiments [25–27]), and (ii) the development of techniques for measuring atom-atom correlations [13,28–34]. Demonstrations of continuous-variable EPR correlations in atomic quadratures will additionally require the measurement of matter-wave quadrature amplitudes using stable, mode-matched local oscillator fields as phase references [21,35]. This is a challenging task yet to be realized experimentally. In the case of fermionic statistics of the constituent atoms, dissociation of a molecular BEC offers

a new paradigm of fermionic quantum atom optics [36,37] and new opportunities for extensions of fundamental tests of quantum mechanics to ensembles of neutral fermionic atoms.

The purpose of this article is a qualitative and quantitative understanding of the simplest density-density and atom number correlations in spontaneous dissociation of a molecular BEC in the short-time limit. Strong atom-atom correlations and relative number squeezing can be regarded as precursors of more complex EPR correlations. In the short-time limit, the converted fraction of molecules into constituent atoms is small and one can employ the undepleted molecular-field approximation, which was successfully used in theoretical descriptions of parametric down-conversion in quantum optics [38]. Even though a less restrictive description of dissociation dynamics can be accomplished via state-of-the-art numerical techniques, such as the first-principles simulations using the positive- P and Gaussian representations [39–43], the truncated Wigner function approach [42], the Hartree-Fock-Bogoliubov method [37,42,44], and a generalized Gross-Pitaevskii (GP) equation [45], the main motivation of the present work is to obtain approximate analytic results which are less computationally expensive and have the intrinsic appeal of analytic simplicity. By comparing these results with the numerical ones, one can verify their accuracy and the range of validity in different parameter regimes. For a related problem of atomic four-wave mixing via condensate collisions [34], a similar analytic treatment has been employed in Ref. [46], with the results in the short-time limit comparing very well with the first-principles simulations in the positive P representation [47].

The main question that we address here is the influence of the spatial inhomogeneity of the source (molecular) condensate on the strength of atom-atom correlations. This is an important problem for modeling realistic experiments performed using trapped, inhomogeneous condensates with interactions. For example, for a harmonically trapped system, the spatial inhomogeneity and the multimode character of the problem enters through the shape of the density profile of the initial condensate which—in the Thomas-Fermi (TF) limit—is close to an inverted parabola. The shape of the source in turn

determines the extent to which the effect of mode-mixing affects the spatial structure of atom-atom correlations. For strong inhomogeneity, the effect can be quite detrimental and can reduce the strength of correlations significantly. Our analytic results allow us to quantify these effects in a relatively simple way, as the short-time limits to correlation functions are obtained in a closed explicit form in terms of Bessel functions. In a recent rapid communication [48], we presented some of these results for dissociation in a one-dimensional (1D) geometry; in the present work, we give the details of derivations and extend the results to 2D and 3D systems.

In addition, our comparison between the results for bosonic and fermionic atoms allows for a demonstration of striking differences in the dissociation dynamics that depend inherently on the difference in quantum statistics. For short durations of dissociation, which produce low-density atomic clouds, these differences are not obstructed by the s -wave scattering interactions and have been recently studied in the context of directionality effects due to Bose enhancement and Pauli blocking in the dissociation of elongated molecular condensates [49].

Related recent studies of molecular dissociation are concerned with the role of confinement on the stability of the molecular BEC [50], the effect of magnetic-field fluctuations and modulations on the dissociation dynamics near a Feshbach resonance [51], the dynamics of dissociation in optical lattices [52], dissociation of molecules prepared in a vortex state [53], connection of dissociation with the generators of the SU(1,1) and SU(2) Lie algebras [54], loss of atom-molecule coherence due to phase diffusion [55], as well as the use of molecular dissociation as a probe of two-body interactions [56], collisional resonances [57], and spectroscopic properties of Feshbach resonance molecules [58,59].

The article is organized as follows. In Sec. II we introduce the model for dissociation of molecular dimers consisting of either two distinguishable bosonic atoms or two fermionic atoms in different spin states. In Sec. III we formulate the same problem for the case of two indistinguishable bosonic atoms. In Sec. IV we present the results of a numerical analysis of molecular dissociation in 1D within the undepleted molecular-field approximation. In Sec. V we develop an analytic approach for the short-time asymptotic behavior and obtain explicit results for the atom-atom pair correlation functions and the relative number squeezing in 1D, 2D, and 3D geometries, for TF and Gaussian density profiles of the molecular BEC. Throughout these sections, we discuss the validity of the approximate model (with no molecular depletion) by comparing the relevant results with those obtained using first-principles positive- P simulations for bosons, in which the molecular-field dynamics and its depletion is treated quantum mechanically. The details of the positive- P method are given in Sec. VI. Finally, in the same Sec. VI we incorporate the effects of s -wave scattering interactions and analyze the system using the truncated Wigner approach. We conclude the article with the summary Sec. VII.

II. DISSOCIATION INTO DISTINGUISHABLE BOSONIC OR FERMIONIC ATOM PAIRS

To model the dissociations of a Bose-Einstein condensate of diatomic molecules into pairs of constituent atoms, we start

with the following effective quantum field theory Hamiltonian, in a rotating frame [60]:

$$\hat{H} = \int d^D \mathbf{x} \left\{ \sum_{i=0,1,2} \frac{\hbar^2}{2m_i} |\nabla \hat{\Psi}_i|^2 + \hbar \Delta (\hat{\Psi}_1^\dagger \hat{\Psi}_1 + \hat{\Psi}_2^\dagger \hat{\Psi}_2) - i\hbar \chi (\hat{\Psi}_0^\dagger \hat{\Psi}_1 \hat{\Psi}_2 - \hat{\Psi}_2^\dagger \hat{\Psi}_1^\dagger \hat{\Psi}_0) \right\}. \quad (1)$$

Here we assume that the molecules [described by the field operator $\hat{\Psi}_0(\mathbf{x}, t)$] are made of either two distinguishable bosonic atoms or two fermionic atoms in different spin states. In both cases, $\hat{\Psi}_0(\mathbf{x}, t)$ is a bosonic field operator satisfying the standard commutation relation $[\hat{\Psi}_0(\mathbf{x}, t), \hat{\Psi}_0^\dagger(\mathbf{x}', t)] = \delta^D(\mathbf{x} - \mathbf{x}')$, with $D = 1, 2$, or 3 corresponding to the dimensionality of the system. The atomic field operators, $\hat{\Psi}_i(\mathbf{x}, t)$ ($i = 1, 2$), satisfy either bosonic commutation or fermionic anti-commutation relations, $[\hat{\Psi}_i(\mathbf{x}, t), \hat{\Psi}_j^\dagger(\mathbf{x}', t)] = \delta_{ij} \delta^D(\mathbf{x} - \mathbf{x}')$ or $\{\hat{\Psi}_i(\mathbf{x}, t), \hat{\Psi}_j^\dagger(\mathbf{x}', t)\} = \delta_{ij} \delta^D(\mathbf{x} - \mathbf{x}')$, depending on the underlying statistics.

The first term in the Hamiltonian (1) describes the kinetic energy where the atomic masses are m_1 and m_2 , whereas the molecular mass is $m_0 = m_1 + m_2$. For simplicity, we consider the case of equal atomic masses (same isotope atoms), with $m_1 = m_2 \equiv m$ and $m_0 = 2m$.

The coupling constant $\chi \equiv \chi_D$ is responsible for coherent conversion of molecules into atom pairs, for example, via optical Raman transitions, an rf transition, or a Feshbach resonance sweep (see, for example, Refs. [60–66] and [67,68] for recent reviews); the microscopic expressions for χ in 1D, 2D, and 3D can be found in Ref. [44].

The detuning Δ is defined to give the overall energy mismatch $2\hbar\Delta$ between the free two-atom state in the dissociation threshold and the bound molecular state (including the relative frequencies of the Raman lasers or the frequency of the rf field; for further details, see Refs. [17,44]). Unstable molecules, spontaneously dissociating into pairs of constituent atoms, correspond to $\Delta < 0$, with $2\hbar|\Delta|$ being the total dissociation energy.

The trapping potential for preparing the initial molecular BEC—with any residual atoms being removed—is omitted from the Hamiltonian since we assume that once the dissociation is invoked, the trapping potential is switched off, so that the dynamics of dissociation is taking place in free space (in 1D and 2D geometries, we assume that the confinement in the eliminated dimensions is kept on so that the free-space dynamics refers only to the relevant dimension under consideration). We assume that the switching on of the atom-molecule coupling and switching off of the trapping potential is done in the regime of a sudden jump [59]. Accordingly, the preparation stage is reduced to assuming a certain initial state of the molecular BEC in a trap, after which the dynamics is governed by the Hamiltonian (1).

In what follows we initially treat the dynamics of dissociation in the undepleted molecular condensate approximation in which the molecules are represented as a fixed classical field. The undepleted molecular approximation is valid for short-enough dissociation times during which the converted fraction of molecules does not exceed $\sim 10\%$ [39,44,49]. In this

regime the dissociation typically produces low-density atomic clouds for which the atom-atom s -wave scattering interactions are negligible [39]; hence, their absence from our Hamiltonian. Additionally, the atom-molecule interactions will initially appear as an effective spatially dependent detuning due to the mean-field interaction energy; this can be neglected by operating at relatively large absolute values of the dissociation detuning $|\Delta|$ so that the total dissociation energy $2\hbar|\Delta|$ dominates the mean-field energy shifts [39,49]. As means of verifying the regime of validity of these approximations, in Sec. VI we incorporate the effects of molecular depletion and s -wave scattering interactions using the positive- P representation and the truncated Wigner method. As these numerical methods are only applicable to bosons, our comparison and conclusions are restricted to the case of dissociation into bosonic atoms. For the case of fermionic atoms, the development of stochastic methods that may facilitate similar comparison in the future are under development [43].

A. Heisenberg equations in the undepleted molecular condensate approximation

The undepleted molecular-field approximation is invoked as follows. Assuming that the molecules are in a coherent state initially, with the density profile $\rho_0(\mathbf{x})$ given by the ground-state solution of the standard GP equation in a harmonic trap, we replace the molecular-field operator by its coherent mean-field amplitude, $\widehat{\Psi}_0(\mathbf{x},0) \rightarrow \langle \widehat{\Psi}_0(\mathbf{x},0) \rangle = \Psi_0(\mathbf{x},0) = \sqrt{\rho_0(\mathbf{x})}$, which we assume is real without loss of generality. We can next introduce an effective, spatially dependent coupling,

$$g(\mathbf{x}) = \chi \sqrt{\rho_0(\mathbf{x})}, \quad (2)$$

and write the Heisenberg equations for the atomic fields as follows:

$$\begin{aligned} \frac{\partial \widehat{\Psi}_1(\mathbf{x},t)}{\partial t} &= i \left[\frac{\hbar}{2m} \nabla^2 - \Delta \right] \widehat{\Psi}_1(\mathbf{x},t) \pm g(\mathbf{x}) \widehat{\Psi}_2^\dagger(\mathbf{x},t), \\ \frac{\partial \widehat{\Psi}_2^\dagger(\mathbf{x},t)}{\partial t} &= -i \left[\frac{\hbar}{2m} \nabla^2 - \Delta \right] \widehat{\Psi}_2^\dagger(\mathbf{x},t) + g(\mathbf{x}) \widehat{\Psi}_1(\mathbf{x},t). \end{aligned} \quad (3)$$

Here and hereafter the $+$ and $-$ signs (in general, upper and lower signs) are for bosonic and fermionic atoms, respectively.

Transforming to Fourier space, $\widehat{\Psi}_j(\mathbf{x},t) = \int d^D \mathbf{k} \widehat{a}_j(\mathbf{k},t) \exp(i\mathbf{k} \cdot \mathbf{x}) / (2\pi)^{D/2}$, where the amplitude operators $\widehat{a}_j(\mathbf{k},t)$ satisfy commutation or anticommutation relations, $[\widehat{a}_i(\mathbf{k}), \widehat{a}_j^\dagger(\mathbf{k}')] = \delta_{ij} \delta^D(\mathbf{k} - \mathbf{k}')$ or $\{\widehat{a}_i(\mathbf{k}), \widehat{a}_j^\dagger(\mathbf{k}')\} = \delta_{ij} \delta^D(\mathbf{k} - \mathbf{k}')$, according to the underlying statistics, we can rewrite Eqs. (3) as a set of linear operator equations:

$$\begin{aligned} \frac{d \widehat{a}_1(\mathbf{k},t)}{dt} &= -i \Delta_k \widehat{a}_1(\mathbf{k},t) \pm \int \frac{d^D \mathbf{q}}{(2\pi)^{D/2}} \widetilde{g}(\mathbf{q} + \mathbf{k}) \widehat{a}_2^\dagger(\mathbf{q},t), \\ \frac{d \widehat{a}_2^\dagger(\mathbf{k},t)}{dt} &= i \Delta_k \widehat{a}_2^\dagger(\mathbf{k},t) + \int \frac{d^D \mathbf{q}}{(2\pi)^{D/2}} \widetilde{g}(\mathbf{q} - \mathbf{k}) \widehat{a}_1(-\mathbf{q},t). \end{aligned} \quad (4)$$

Here

$$\widetilde{g}(\mathbf{k}) = \frac{1}{(2\pi)^{D/2}} \int d^D \mathbf{x} e^{-i\mathbf{k} \cdot \mathbf{x}} g(\mathbf{x}), \quad (5)$$

is the Fourier transform of the effective coupling $g(\mathbf{x})$, and we have defined $\Delta_k \equiv \hbar k^2 / (2m) + \Delta$, where $k = |\mathbf{k}|$.

The general structure of solutions following from Eqs. (4), with vacuum initial conditions for the atomic fields, can be easily understood if we rewrite these operator equations in terms of ordinary differential equations for all possible second-order moments of the atomic field operators. By doing so, one can show that the equations for the normal and anomalous densities, $\langle \widehat{a}_j^\dagger(\mathbf{k},t) \widehat{a}_j(\mathbf{k}',t) \rangle$ and $\langle \widehat{a}_1(\mathbf{k},t) \widehat{a}_2(\mathbf{k}',t) \rangle$, together with their complex conjugates, form a closed set and develop nonzero populations from the δ -function ‘‘seed’’ terms that originate from the following identity: $\langle \widehat{a}_j(\mathbf{k},t) \widehat{a}_j^\dagger(\mathbf{k}',t) \rangle = \delta^D(\mathbf{k} - \mathbf{k}') \pm \langle \widehat{a}_j^\dagger(\mathbf{k},t) \widehat{a}_j(\mathbf{k}',t) \rangle$. The other second-order moments, $\langle \widehat{a}_1^\dagger(\mathbf{k},t) \widehat{a}_2(\mathbf{k}',t) \rangle$ and $\langle \widehat{a}_j(\mathbf{k},t) \widehat{a}_j(\mathbf{k}',t) \rangle$, also form a closed set; however, they never develop nonzero populations if the populations were absent initially. According to this structure, the only nonzero second-order moments are the normal and anomalous densities

$$n_j(\mathbf{k},\mathbf{k}',t) \equiv \langle \widehat{a}_j^\dagger(\mathbf{k},t) \widehat{a}_j(\mathbf{k}',t) \rangle, \quad j = 1,2, \quad (6)$$

$$m_{12}(\mathbf{k},\mathbf{k}',t) \equiv \langle \widehat{a}_1(\mathbf{k},t) \widehat{a}_2(\mathbf{k}',t) \rangle, \quad (7)$$

with $n_1(\mathbf{k},\mathbf{k}',t) = n_2(\mathbf{k},\mathbf{k}',t)$, whereas $\langle \widehat{a}_1^\dagger(\mathbf{k},t) \widehat{a}_2(\mathbf{k}',t) \rangle = 0$ and $\langle \widehat{a}_j(\mathbf{k},t) \widehat{a}_j(\mathbf{k}',t) \rangle = 0$. Since the effective Hamiltonian corresponding to Eqs. (3) is quadratic in the field operators, any higher-order moments or expectation values of products of creation and annihilation operators will factorize according to Wick’s theorem into products of the normal and anomalous densities $n_j(\mathbf{k},\mathbf{k}',t)$ and $m_{12}(\mathbf{k},\mathbf{k}',t)$.

III. DISSOCIATION INTO INDISTINGUISHABLE BOSONIC ATOMS

For completeness, we also analyze dissociation of a BEC of molecular dimers made of pairs of indistinguishable bosonic atoms in the same spin state. This is described by the following effective Hamiltonian [61], in a rotating frame:

$$\begin{aligned} \widehat{H} &= \int d^D \mathbf{x} \left\{ \sum_{i=0,1} \frac{\hbar^2}{2m_i} |\nabla \widehat{\Psi}_i|^2 + \hbar \Delta \widehat{\Psi}_1^\dagger \widehat{\Psi}_1 \right. \\ &\quad \left. - i \frac{\hbar \chi}{2} (\widehat{\Psi}_0^\dagger \widehat{\Psi}_1^2 - \widehat{\Psi}_1^\dagger \widehat{\Psi}_0) \right\}. \end{aligned} \quad (8)$$

Here $\widehat{\Psi}_1(\mathbf{x},t)$ is the atomic field operator, χ is the respective atom-molecule coupling [44,64], m_0 and $m_1 \equiv m$ are, respectively, the molecular and atomic masses ($m_0 = 2m$), and Δ is the detuning corresponding to the total dissociation energy of $2\hbar|\Delta|$.

The treatment of this system is essentially the same as in the previous case of distinguishable atoms, except that the field operators $\widehat{\Psi}_2^\dagger(\mathbf{x},t)$ and $\widehat{a}_2^\dagger(\mathbf{k},t)$ in Eqs. (3) and (4) are replaced, respectively, with $\widehat{\Psi}_1^\dagger(\mathbf{x},t)$ and $\widehat{a}_1^\dagger(\mathbf{k},t)$. The corresponding Heisenberg equations now read as

$$\frac{\partial \widehat{\Psi}_1(\mathbf{x},t)}{\partial t} = i \left[\frac{\hbar \nabla^2}{2m} - \Delta \right] \widehat{\Psi}_1(\mathbf{x},t) + g(\mathbf{x}) \widehat{\Psi}_1^\dagger(\mathbf{x},t) \quad (9)$$

and

$$\frac{d \widehat{a}_1(\mathbf{k},t)}{dt} = -i \Delta_k \widehat{a}_1(\mathbf{k},t) + \int \frac{d^D \mathbf{q}}{(2\pi)^{D/2}} \widetilde{g}(\mathbf{q} + \mathbf{k}) \widehat{a}_1^\dagger(\mathbf{q},t), \quad (10)$$

whereas the nonzero normal and anomalous densities are given by

$$n_1(\mathbf{k}, \mathbf{k}', t) \equiv \langle \hat{a}_1^\dagger(\mathbf{k}, t) \hat{a}_1(\mathbf{k}', t) \rangle, \quad (11)$$

$$m_{11}(\mathbf{k}, \mathbf{k}', t) \equiv \langle \hat{a}_1(\mathbf{k}, t) \hat{a}_1(\mathbf{k}', t) \rangle, \quad (12)$$

where we have omitted the atomic spin index for notational simplicity.

IV. NUMERICAL RESULTS AND DISCUSSION

In our numerical treatment of the problem (present section) we only consider a 1D system. This is to make the problem computationally tractable. However, based on the physical understanding that we develop, we expect our results to be at least qualitatively valid for 3D systems, as is the case for a 2D problem treated recently in Ref. [49]. The analytical results of Sec. V, on the other hand, are obtained for 1D, 2D, and 3D systems.

From the structure of Eqs. (4) we can easily recognize the role of mode-mixing in the spatially inhomogeneous treatment compared to the case of a uniform molecular condensate. In the uniform case, the Fourier transform of the effective coupling g_0 is a δ function $\tilde{g}(\mathbf{k}) = (2\pi)^{D/2} g_0 \delta(\mathbf{k})$, so that the operator $\hat{a}_1(\mathbf{k})$ couples to the conjugate of the partner spin component at exactly the opposite momentum, $\hat{a}_2^\dagger(-\mathbf{k})$. Therefore, the entire set of coupled equations breaks down into pairs of equations that couple only the opposite momentum components of the two atomic fields with different spins. Accordingly, only the diagonal and antidiagonal terms of the normal and anomalous densities, $n_j(\mathbf{k}, \mathbf{k})$ and $m_{12}(\mathbf{k}, -\mathbf{k})$, develop nonzero populations as the dissociation proceeds.

In the present inhomogeneous case, on the other hand, the finite width of the effective coupling $\tilde{g}(\mathbf{k})$ implies that $\hat{a}_1(\mathbf{k})$ couples not only to $\hat{a}_2^\dagger(-\mathbf{k})$ in Eq. (4), but also to a range of momenta in the neighborhood of $-\mathbf{k}$, within $-\mathbf{k} \pm \delta\mathbf{k}$. This is the origin of mode-mixing. The spread in $\delta\mathbf{k}$ determines the width of the pair correlation between the atoms in the two opposite spin states that have equal but opposite momenta. The width is ultimately related to the momentum width of the source molecular condensate, as we show later in this article.

At a qualitative level, the finite width of the pair correlation at opposite momenta can be understood from a simple momentum conservation argument. For a molecule at rest, the dissociation produces one atom in each spin state satisfying $\mathbf{k}_1 + \mathbf{k}_2 = 0$, and therefore $\mathbf{k}_2 = -\mathbf{k}_1$. From energy conservation $2\hbar|\Delta| = (\hbar^2|\mathbf{k}_1|^2 + \hbar^2|\mathbf{k}_2|^2)/2m$, the absolute momentum of each atom is given by $k_0 = |\mathbf{k}_1| = |\mathbf{k}_2| = \sqrt{2m|\Delta|/\hbar}$. The same momentum conservation holds in the center-of-mass frame of the molecule if it has a finite momentum offset $\delta\mathbf{k}$ due to the initial momentum spread of the condensate. In the laboratory frame, this center-of-mass momentum offset leads to an offset from $\pm\mathbf{k}_0$ in the momenta of dissociated atoms, $\mathbf{k}_1 = \mathbf{k}_0 + \delta\mathbf{k}/2$ and $\mathbf{k}_2 = -\mathbf{k}_0 + \delta\mathbf{k}/2$. This implies that a pair of atom detectors set to detect atoms with these momenta will produce a positive pair correlation signal and will therefore contribute to the finite width of the order of $\delta\mathbf{k}$ in the density-density correlation function [69].

We now turn to the quantitative analysis of atom-atom correlations. Before we proceed, however, we discuss the

role of mode-mixing on simpler observables—the atomic momentum distribution and mode population dynamics in the two spin states.

A. Momentum distribution and mode population dynamics

In a finite quantization volume, the wave vector \mathbf{k} is discrete and the plane-wave mode annihilation and creation operators $\hat{a}_{j,\mathbf{k}} = \hat{a}_j(\mathbf{k}, t)(\Delta k_x \Delta k_y \Delta k_z)^{1/2}$ and $\hat{a}_{j,\mathbf{k}}^\dagger = \hat{a}_j^\dagger(\mathbf{k}, t)(\Delta k_x \Delta k_y \Delta k_z)^{1/2}$ (where $j = 1, 2$ and $\Delta k_{x,y,z}$ are the lattice spacings in x , y , and z directions) may be organized into a vector \hat{a} . The Heisenberg equations (4) may then be written in vector-matrix form as $d\hat{a}/dt = \mathbf{M}\hat{a}$, where \mathbf{M} is a square matrix of complex numbers of dimension equal to twice the total number of lattice points. The solutions of these linear operator equations can be found by numerically computing the matrix exponential $\exp(\mathbf{M}t)$. The task is relatively simple in 1D, which is the case that we present here.

In our numerical analysis, we consider three typical examples of the density profiles $\rho_0(x)$ of the molecular BEC, corresponding to relatively weak, intermediate, and strong inhomogeneity. These are shown in Fig. 1 and correspond to having different frequencies of the longitudinal trapping potential along x and the same peak density $\rho_0 \equiv \rho_0(0)$. The density profiles shown are given by the ground-state solution of the 1D GP equation in a harmonic trap and can be closely approximated by a TF inverted parabola $\rho_0(x) = \rho_0(1 - x^2/R_{\text{TF}}^2)$ for $|x| < R_{\text{TF}}$ and $\rho_0(x) = 0$ elsewhere; the three examples shown correspond to the TF radii of $R_{\text{TF}} = 250 \mu\text{m}$, $R_{\text{TF}} = 167 \mu\text{m}$, and $R_{\text{TF}} = 83 \mu\text{m}$.

To allow for a comparison of the present nonuniform treatment with the known analytic solutions of a uniform model [36], we also show a uniform box system (dashed line in Fig. 1), which is size-matched with the largest trapped system, curve (1). We choose the size-matched uniform box to have the same uniform density ρ_u as the peak density ρ_0

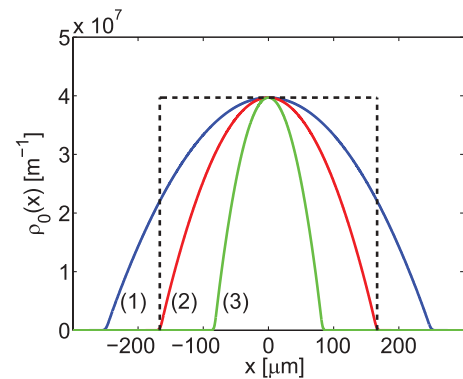


FIG. 1. (Color online) Molecular BEC density profiles $\rho_0(x)$ as ground-state solutions of the Gross-Pitaevskii equation in a harmonic trap with longitudinal frequencies $\omega/2\pi = 1, 3/2$, and 3 Hz represented, respectively, by the curves (1), (2), and (3). In the Thomas-Fermi (TF) regime, the corresponding TF radii are (1) $R_{\text{TF}} \simeq 250 \mu\text{m}$, (2) $R_{\text{TF}} \simeq 167 \mu\text{m}$, and (3) $R_{\text{TF}} \simeq 83 \mu\text{m}$. The dashed box illustrates a uniform system which is size matched with the inhomogeneous system (1). Other physical parameters are given in Ref. [70].

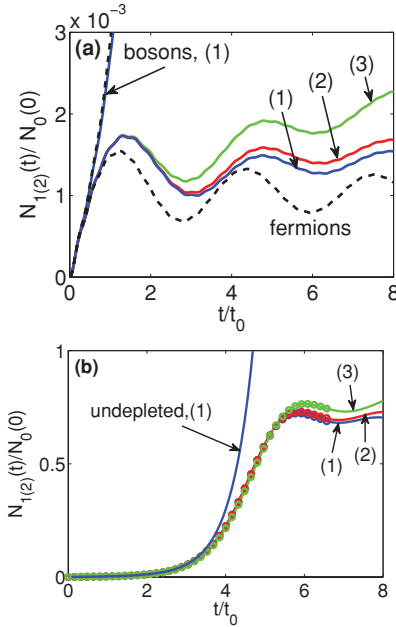


FIG. 2. (Color online) (a) Total fractional number of atoms $N_j(t)/N_0(0)$ [$N_1(t) = N_2(t)$] as a function of time t/t_0 in one of the spin components in dissociation into fermionic or bosonic atoms. The different curves (1), (2), and (3) correspond to dissociation of molecular BECs having density profiles as indicated in Fig. 1, with the dashed line referring to the uniform case. The results are obtained within the undepleted molecular approximation. The dimensionless detuning $\delta = \Delta t_0$ is $\delta = -9$, where the time scale is $t_0 = 1/\chi\sqrt{\rho_0}$. For $\chi = 3.15 \times 10^{-2} \text{ m}^{1/2}/\text{s}$ and $\rho_0 = 4 \times 10^7 \text{ m}^{-1}$, the time scale would be $t_0 = 5 \text{ ms}$. Accordingly, the absolute detuning is $|\Delta| = 1800 \text{ s}^{-1}$ and the resonant momentum is $k_0 = \sqrt{2m|\Delta|/\hbar} \simeq 1.5 \times 10^6 \text{ m}^{-1}$ in the present example [70]. (b) Total fractional numbers of bosonic atoms $N_j(t)/N_0(0)$ from numerical simulations that take into account molecular depletion. The different curves are as in (a), with the curve (1) from the undepleted molecular approximation shown for comparison. The solid curves are from the truncated Wigner method, while the circles are from the exact positive- P method (see Sec. VI), which in this example is limited to simulation duration of $t/t_0 \sim 6.5$ due to the growing sampling errors.

of the nonuniform system and the same total initial number of molecules N_0 . For a simple TF parabola, N_0 is given by $N_0 = 4\rho_0 R_{\text{TF}}/3$, while for the box system $N_0 = \rho_u L$, and therefore we require that the box length is $L = 4R_{\text{TF}}/3$.

In Fig. 2(a) we plot the total number of atoms in each spin component,

$$N_j(t) = \int dk n_j(k, t), \quad (13)$$

where

$$n_j(k, t) = n_j(k, k, t) = \langle \hat{a}_j^\dagger(k, t) \hat{a}_j(k, t) \rangle \quad (14)$$

is the density distribution in momentum space. The three curves (1), (2), and (3) referring to fermionic atoms correspond, respectively, to dissociation of molecular condensates with the density profiles shown Fig. 1. Plotted are the fractional atom numbers, $N_j(t)/N_0(0)$ [with $N_1(t) = N_2(t)$], where $N_0(0)$ in each case is the respective total initial number of molecules. For comparison, we also show the result for

bosonic atoms corresponding to the molecular density profile (1). The two dashed curves are the respective (fermionic or bosonic) results for a uniform system, size matched with the molecular condensate profile (1).

The differences among the curves (1), (2), and (3) demonstrate the strong dependence of the dissociation dynamics on the inhomogeneity of the initial molecular condensate. We note that all fermionic examples are in the parameter regime where the dynamics is dominated by Pauli blocking of individual atomic modes rather than by molecular depletion [44]. Accordingly, only a small fraction of molecules is converted into atoms and this justifies the use of the undepleted molecular approximation for longer time scales than in the respective bosonic systems.

In Fig. 2(b) we show the results of numerical simulations that go beyond the undepleted molecular approximation. The simulations are performed for dissociation into bosonic atoms using the positive- P representation and the truncated Wigner methods (see Sec. VI for further details). They take into account the conversion dynamics and quantum fluctuations of the molecular field, in contrast to the results of Fig. 2(a). As we see, the results of the undepleted molecular approximation are in excellent agreement with the exact positive- P results for dissociation durations up to $t/t_0 \sim 3.5$ corresponding to more than 10% conversion. At later times, the exact results show the slowing down of the atom number growth due to the depletion of the molecular condensate, followed by the reverse process of atom-atom recombination into molecules.

To further illustrate the differences between the uniform and nonuniform results, we plot in Fig. 3 the momentum distribution of the dissociated fermionic atoms, $n_j(k, t)$, as a function of time. The distribution is symmetric around the origin and has two peaks centered around the resonant momenta $k = \pm k_0$; in Fig. 3 we only show the spectrum around $k = k_0$. Qualitatively, the momentum distribution is similar to the one obtained within the uniform treatment except that the oscillation of the resonant momentum is no longer periodic and the minima do not reach zero [36,44]. We recall that in the uniform case the oscillations of different plane-wave mode

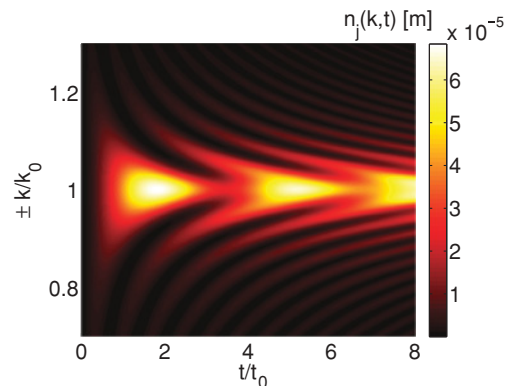


FIG. 3. (Color online) Atomic momentum distribution $n_j(k, t)$ [$n_1(k, t) = n_2(k, t)$] in one of the spin components for dissociation into fermionic atoms, as a function of a scaled time t/t_0 . The example is for the molecular BEC profile corresponding to the case (1) in Fig. 1. The dimensionless detuning is $\delta = -9$, as in Fig. 2.

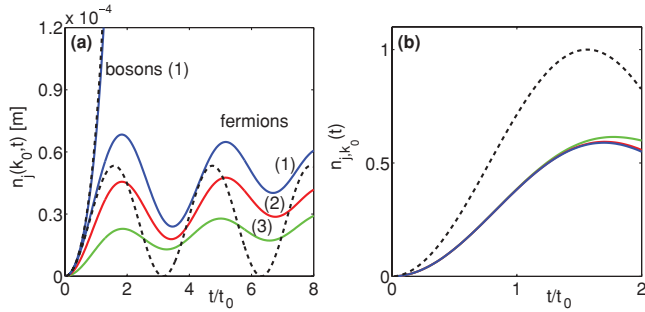


FIG. 4. (Color online) (a) Peak density $n_j(k_0, t)$ [$n_1(k_0, t) = n_2(k_0, t)$] as a function of time t/t_0 in one of the spin components in dissociation into fermionic or bosonic atoms. The three different curves for fermions correspond to the molecular BEC profiles (1), (2), and (3) of Fig. 1, while the oscillating dashed curve is the peak atomic density for a uniform system that is size matched with (1). The bosonic curve together with the respective dashed curve for a size-matched uniform system is for the molecular BEC profile (1) of Fig. 1. The dimensionless detuning is the same as in Fig. 2, $\delta = -9$. (b) Comparison of the average mode *occupancy* in the uniform fermionic system (dashed curve) and the respective nonuniform systems (solid curves), corresponding to cases (1), (2), and (3) of Fig. 1. The latter three curves are almost indistinguishable from each other on this scale.

occupancies are periodic and are given by [36]

$$n_{j,k}(t) = \frac{g_0^2}{g_0^2 + \Delta_k^2} \sin^2\left(\sqrt{g_0^2 + \Delta_k^2} t\right), \quad (15)$$

where $g_0 \equiv g(0)$ is the effective coupling and $\Delta_k \equiv \hbar k^2/(2m) + \Delta = \hbar(k^2 - k_0^2)/2m$. In the bosonic case, we find that the density distributions are closer to the respective uniform results of Refs. [36,39], $n_{j,k}(t) = [g_0^2/(g_0^2 - \Delta_k^2)] \sinh^2(\sqrt{g_0^2 - \Delta_k^2} t)$, and we do not show them here.

In Fig. 4(a) we monitor the atomic density at the resonant momentum k_0 as a function of time; the three fermionic curves correspond, respectively, to the molecular density profiles (1), (2), and (3) of Fig. 1, whereas the oscillatory dashed line corresponds to the analytic solution for a size-matched uniform system (1). The analytic result represents the density distribution $n_j(k_0, t)$ and is obtained from the average occupation number of the resonant mode, $n_{j,k_0}(t) = \sin^2(g_0 t)$, by converting it into the density distribution via $n_j(k_0, t) = n_{j,k_0}(t)/\Delta k$, where $\Delta k = 2\pi/L$ is the mode spacing of the size-matched uniform system of length L . The respective bosonic results for the largest molecular BEC are also shown for comparison; in this case the uniform analytic result for the resonant mode is given by $n_{j,k_0}(t) = \sinh^2(g_0 t)$ [36,39] and grows exponentially with time due to Bose stimulation.

An alternative way of comparing the results for the uniform and nonuniform systems is to define the physical “modes” of the nonuniform system and to compare their average occupation numbers with those obtained in the uniform finite size box. In the latter case, the natural modes of the system are the plane-wave modes which coincide with our computational lattice modes. In the case of dissociation into fermionic atoms, the plane-wave mode occupation numbers are bound to be no more than 1 by the Pauli exclusion principle [36]. In the nonuniform system, on the other hand, the plane-wave

modes are not the natural modes of the system and therefore care should be taken when defining the physical modes and discussing the Pauli exclusion principle. Following Glauber’s theory of optical coherence in the context of matter waves [71], we define the atomic “mode” in the nonuniform system using the first-order coherence length, $\Delta k^{(\text{coh})}$, which in turn is defined via the first-order correlation function

$$g_{jj}^{(1)}(k, k', t) = \frac{\langle \hat{a}_j^\dagger(k, t) \hat{a}_j(k', t) \rangle}{\sqrt{n_j(k, t) n_j(k', t)}}. \quad (16)$$

More specifically, we define $\Delta k^{(\text{coh})}$ as the distance $|k - k'|$ over which $|g_{jj}^{(1)}(k, k', t)|$ reduces by a factor of 2 from its peak value at $k - k' = 0$. The average mode occupation is then given by $n_{j,k}(t) = n_j(k, t) \Delta k^{(\text{coh})}$. In Fig. 4(b) we plot $n_{j,k_0}(t)$, defined in this way, and compare it with the occupancies of the plane-wave modes of the uniform system (dashed line). As we see, the mode occupancy in the nonuniform system deviates substantially from the uniform result and remains below the maximum occupancy of 1. We note that the nonuniform results corresponding to cases (1), (2), and (3) of Fig. 1 almost coincide with each other and the respective three curves in Fig. 4(b) are almost indistinguishable until the first oscillation maximum. This implies that the mode occupation dynamics depends only on the shape of the molecular condensate and not on its size, at least in the short-time limit. [For example, for a Gaussian shape of the molecular condensate, we find that the mode occupation dynamics is slightly different.] In the longer time limit, the first-order correlation function in the fermionic case develops complicated multipeak structure (similar to the one seen in the momentum distribution of Fig. 3). In this case, defining the first-order coherence length $\Delta k^{(\text{coh})}$ as the half-width at half maximum becomes less appropriate since this definition ignores the correlation peaks at large $|k - k'|$.

Even though we do not present explicit numerical results for the first-order correlation function itself, we point out that in the present model the absolute value of $g_{jj}^{(1)}(k, k', t)$ is related to the second-order correlation function $g_{jj}^{(2)}(k, k', t)$ via

$$|g_{jj}^{(1)}(k, k', t)| = \sqrt{|g_{jj}^{(2)}(k, k', t) - 1|}. \quad (17)$$

We now turn to the analysis of the second-order correlation functions for pairs of atoms in the same spin state, $g_{jj}^{(2)}(k, k', t)$ ($j = 1, 2$), and in the opposite spin states, $g_{12}^{(2)}(k, k', t)$.

B. Atom-atom correlations

1. Distinguishable fermionic or bosonic atoms

Since the dissociation of diatomic molecules produces pairs of atoms in two different spin states which fly apart in opposite directions according to the momentum conservation, we expect strong correlation signal for atom pairs with nearly equal but opposite momenta. We refer to this type of correlation as back-to-back (BB) correlation and quantify it via Glauber’s second-order correlation function,

$$g_{12}^{(2)}(k, k', t) = \frac{\langle \hat{a}_1^\dagger(k, t) \hat{a}_2^\dagger(k', t) \hat{a}_2(k', t) \hat{a}_1(k, t) \rangle}{\langle \hat{a}_1^\dagger(k, t) \hat{a}_1(k, t) \rangle \langle \hat{a}_2^\dagger(k', t) \hat{a}_2(k', t) \rangle}. \quad (18)$$

Apart from the normal ordering of the creation and annihilation operators, the pair correlation function $g_{12}^{(2)}(k, k', t)$ describes the density-density correlation between the momentum components k and k' of pairs of atoms in the two spin states. The normalization with respect to the product of individual densities $n_j(k, t) = \langle \hat{a}_j^\dagger(k, t) \hat{a}_j(k, t) \rangle$ ensures that for uncorrelated states $g_{12}^{(2)}(k, k', t) = 1$. Due to obvious symmetry considerations, $g_{12}^{(2)}(k, k', t) = g_{21}^{(2)}(k, k', t)$.

The second type of correlation expected to be present in the system is between pairs of atoms in the same spin state, propagating with the nearly same momenta, $k \simeq k'$. This type of correlation, which we refer to as collinear (CL) correlation, is due to quantum statistical effects and represents a manifestation of the Hanbury Brown and Twiss (HBT) effect [28,32,72]. The CL correlations are quantified via the following second-order correlation function:

$$g_{jj}^{(2)}(k, k', t) = \frac{\langle \hat{a}_j^\dagger(k, t) \hat{a}_j^\dagger(k', t) \hat{a}_j(k', t) \hat{a}_j(k, t) \rangle}{\langle \hat{a}_j^\dagger(k, t) \hat{a}_j(k, t) \rangle \langle \hat{a}_j^\dagger(k', t) \hat{a}_j(k', t) \rangle}. \quad (19)$$

The linearity of Eqs. (4) ensures that one can apply Wick's theorem to Eqs. (18) and (19) and factorize the fourth-order operator moments into the sum of products of second-order moments. Noting in addition that $\langle \hat{a}_1^\dagger(k, t) \hat{a}_2(k', t) \rangle = 0$ and $\langle \hat{a}_j(k, t) \hat{a}_j(k', t) \rangle = 0$ in the present model, we obtain the following results for the BB and CL correlations:

$$g_{12}^{(2)}(k, k', t) = 1 + \frac{|m_{12}(k, k', t)|^2}{n_1(k, t)n_2(k', t)}, \quad (20)$$

$$g_{jj}^{(2)}(k, k', t) = 1 \pm \frac{|n_j(k, k', t)|^2}{n_j(k, t)n_j(k', t)}, \quad (21)$$

where the + and - signs stand for bosonic and fermionic atoms, respectively.

The BB pair correlation $g_{12}^{(2)}(k, k_0, t = t_0)$ in which the momentum of one of the atomic spin components is fixed to the resonant momentum k_0 , while the momentum k of the opposite spin component is being varied is plotted in Fig. 5(a). The two curves correspond to the fermionic and bosonic atom statistics, as indicated by the labels. In both cases, we see a clear correlation peak at $k = -k_0$ corresponding to atom pairs with equal but opposite momenta ($k_0, -k_0$). The width of the correlation is discussed in Sec. IV C.

The major quantitative difference between the present nonuniform result and that of a uniform system is that the peak value of the BB correlation $g_{12}^{(2)}(-k_0, k_0, t)$ becomes smaller than in the uniform system and that the correlation function acquires a finite width. As has been shown in Refs. [36,44], the strength of the pair correlation in the uniform system corresponds to its maximum possible value for a given occupancy $n_{1, k_0}(t) = n_{2, k_0}(t)$. More specifically, the pair correlation upper bound is given by $g_{12}^{(2)}(-k_0, k_0, t) = 1/n_{1, k_0}(t)$ in the case of fermionic atoms and $g_{12}^{(2)}(-k_0, k_0, t) = 2 + 1/n_{1, k_0}(t)$ in the bosonic case, whereas $g_{12}^{(2)}(k, k_0, t) = 1$ for any $k \neq -k_0$ in both cases. In other words, the pair correlation in the uniform system is a Kronecker-like δ function, whereas in the nonuniform case it acquires a finite width and the peak value is reduced.

Given that $n_{j, k_0}(t)$ in the uniform system is an oscillatory function for fermions and can reach zero values at

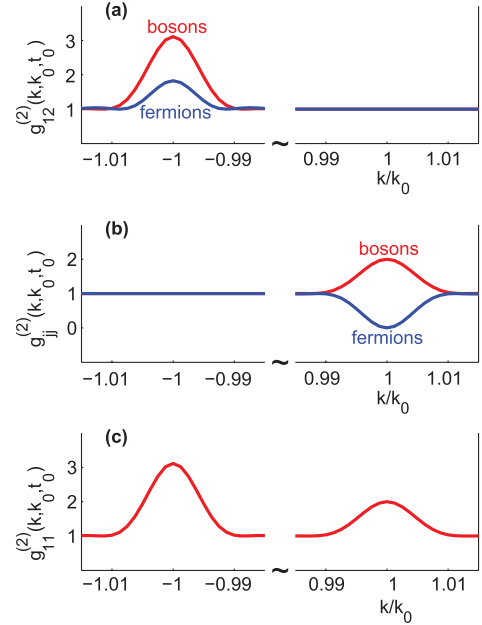


FIG. 5. (Color online) Atom-atom pair correlations at $t/t_0 = 1$ for the case of the molecular BEC profile (1) in Fig. 1 and dimensionless detuning $\delta = -9$. (a) $g_{12}^{(2)}(k, k_0, t_0)$ as a function of k for fermionic and bosonic atom pairs in two different spin states, showing the peak corresponding to strong back-to-back correlation around $k = -k_0$. (b) Pair correlation for the same-spin atoms $g_{11}^{(2)}(k, k_0, t_0)$ in dissociation into distinguishable (fermionic or bosonic) atom pairs, showing a peak (bosons) or a dip (fermions) at $k = k_0$, which correspond, respectively, to bosonic bunching due to Bose stimulation or fermionic antibunching due to Pauli blocking. (c) Pair correlation $g_{11}^{(2)}(k, k_0, t_0)$ in dissociation into indistinguishable (same spin state) bosonic atom pairs, showing both back-to-back and CL correlation signals at $k = -k_0$ and $k = k_0$.

certain times, the respective BB correlation $g_{12}^{(2)}(-k_0, k_0, t) = 1/n_{1, k_0}(t)$ is discontinuous [$g_{12}^{(2)}(-k_0, k_0, t) \rightarrow \infty$] whenever $n_{j, k_0}(t) \rightarrow 0$. In contrast to this unphysical result, the peak value of the BB correlation in the nonuniform system is always continuous and is shown in Fig. 6. The oscillatorylike structure of the BB correlation for fermions comes from the oscillatory behavior of the atomic density $n_j(k, t)$ and the absolute value of the anomalous density $|m_{12}(k_0, -k_0, t)|$. The oscillations in $|m_{12}(k_0, -k_0, t)|$ resemble those for a uniform system [36], with $|m_{k_0, -k_0}(t)|^2 = n_{j, k_0}(t)[1 - n_{j, k_0}(t)]$, except that here they do not reach the minimum and maximum values corresponding to perfect harmonic oscillations in $n_{j, k_0}(t)$. The BB correlation for the case of bosonic atoms is also shown on the same figure (solid red curve) and does not display any oscillations. We note that the bosonic curve should have been stopped at $t/t_0 \sim 3$ as the undepleted molecular approximation breaks down beyond $t/t_0 \gtrsim 3$ (the total number of atoms produced beyond this point in time corresponds to a conversion of more than 10% of the initial number of molecules), while this is not the case for fermionic atoms. We extend the bosonic curve to $t/t_0 \sim 5$ in order to make visible its discrepancy with the numerical results based on the exact positive- P representation (red circles) and the truncated Wigner method (red dash-dotted curve).

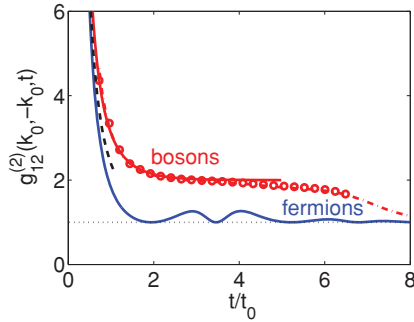


FIG. 6. (Color online) Back-to-back pair correlations $g_{12}^{(2)}(-k_0, k_0, t)$ at equal but opposite peak momenta as a function of time t/t_0 for dissociation into fermionic (blue solid curve) and bosonic (red solid curve) atoms in two spin states from the numerical simulations within the undepleted molecular-field approximation. The results are for the molecular density profiles corresponding to case (1) in Fig. 1. The dimensionless detuning is $\delta = -9$ as in Fig. 2. The dashed (black) curve is the short-time analytic result of Eq. (38) from Sec. V; the curve is extended to time duration of $t/t_0 \sim 1$, which, strictly speaking, is beyond the expected validity of the perturbative theory, $t/t_0 \ll 1$, yet we see a reasonably good agreement with the numerical results for $t/t_0 \sim 1$. The dash-dotted (red) curve is from the truncated Wigner approach, while the red circles are from the exact positive- P method; both methods take into account the molecular-field depletion (see Sec. VI for details). As we see the result from the undepleted molecular-field approximation (solid red curve, bosons) are in excellent agreement with the positive- P and truncated Wigner results for durations up to $t/t_0 \sim 5$.

The CL correlation function $g_{11}^{(2)}(k, k_0, t)$ [with $g_{11}^{(2)}(k, k_0, t) = g_{22}^{(2)}(k, k_0, t)$] at $t = t_0$ is plotted in Fig. 5(b) as a function of k . In the case of bosonic atoms we see the expected HBT peak at $k = k_0$, with $g_{11}^{(2)}(k_0, k_0, t) = 2$ due to bosonic stimulation. In the fermionic case, on the other hand, we see a dip $g_{11}^{(2)}(k_0, k_0, t) = 0$ corresponding to fermionic antibunching due to Pauli blocking. The physics behind these effects is the same as the CL correlations between the s -wave scattered atoms in a collision of two condensates of metastable $^4\text{He}^*$ atoms as observed in Ref. [34] and the local correlations in a thermal cloud of bosonic $^4\text{He}^*$ atoms and an ultracold cloud of fermionic $^3\text{He}^*$ atoms as observed in Refs. [32] (see also [28]).

2. Indistinguishable bosonic atoms

In the case of dissociation of molecules made of bosonic atom pairs in the same spin state, the atom-atom pair correlation function is given by

$$g_{11}^{(2)}(k, k', t) = \frac{\langle \hat{a}_1^\dagger(k, t) \hat{a}_1^\dagger(k', t) \hat{a}_1(k', t) \hat{a}_1(k, t) \rangle}{\langle \hat{a}_1^\dagger(k, t) \hat{a}_1(k, t) \rangle \langle \hat{a}_1^\dagger(k', t) \hat{a}_1(k', t) \rangle} = 1 + \frac{|n_1(k, k', t)|^2 + |m_{11}(k, k', t)|^2}{n_1(k, t) n_1(k', t)}. \quad (22)$$

Here, the BB correlation signal comes from the anomalous density term $|m_{11}(k, k', t)|^2$ as it is nonzero only for pairs of momenta k and k' that are nearly opposite, whereas the normal density term $|n_1(k, k', t)|^2$ is vanishingly small for opposite pairs of momenta. On the other hand, the CL correlation signal

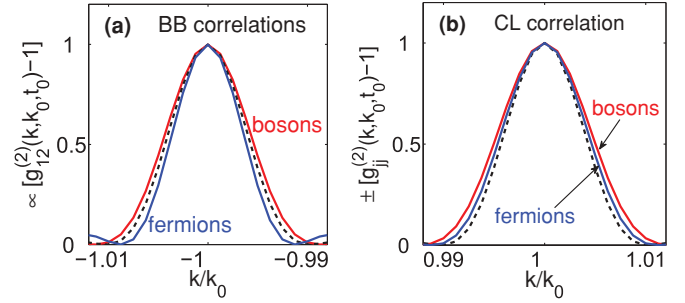


FIG. 7. (Color online) (a) Back-to-back pair correlation functions, $g_{12}^{(2)}(k, k_0, t_0)$, at time $t = t_0$ for fermions (blue solid curve) and bosons (red solid curve), corresponding to the molecular BEC profile (1) of Fig. 1. The magnitudes of the correlation functions are scaled to 1 in order to simplify the comparison of the correlation widths and the width of the source (dashed curve), that is, the momentum distribution of the molecular BEC. (b) CL pair correlation functions, $g_{jj}^{(2)}(k, k_0, t_0)$, for fermions (blue solid curve) and bosons (red solid curve), for the same parameters as in (a). The fermionic curve for $g_{jj}^{(2)}(k, k_0, t_0) - 1$ is inverted to allow for the comparison of the correlation widths. The dashed curve is the momentum distribution of the source.

comes from the normal density term $|n_1(k, k', t)|^2$ which is nonzero for pairs of nearby momenta, while the anomalous density is vanishingly small when $k \simeq k'$.

In Fig. 5(c) we plot the pair correlation $g_{11}^{(2)}(k, k_0, t_0)$ as a function of k , and we see the simultaneous presence of two peaks: one at $k = -k_0$ representing the BB correlation due to the momentum conserving pair-production process and the second peak at $k = k_0$ corresponding to the HBT effect.

C. Width of the correlation functions

An important observable in the experiments on atom-atom correlations is the width of the correlation functions. Here we discuss the BB and CL correlation widths during relatively short durations of dissociation, corresponding to the range of validity of the undepleted molecular-field approximation.

In Fig. 7 we show the numerical results for the BB and CL correlations functions at time $t = t_0$ and compare them with the shape of the source molecular BEC in momentum space. The results correspond to the molecular BEC density profile (1) of Fig. 1. We see that in the short-time limit the width and the overall shape of the correlation functions for both fermionic and bosonic atoms is determined essentially by the width and the shape of the momentum distribution of the source molecular BEC.

For quantitative purposes we define the widths as the half-width at half maximum and denote them $w^{(\text{BB})}$ and $w^{(\text{CL})}$ for the back-to-back and for CL correlations, respectively. The width of the source molecular BEC in momentum space is denoted as w . The widths of the BB and CL correlations relative to the source width as a function of time are shown in Fig. 8. The source condensate here corresponds to the molecular BEC profile (1) of Fig. 1, having the momentum width of $w \simeq 1.62/R_{\text{TF}}$, where R_{TF} is the respective TF radius in x space. We see that the BB correlation width starts from the asymptotic value of $w^{(\text{BB})} = w$, corresponding to the limit $t \rightarrow 0$, and grows slowly for bosons and decreases for fermions. A similar behavior is seen in the CL correlation width, except that it starts

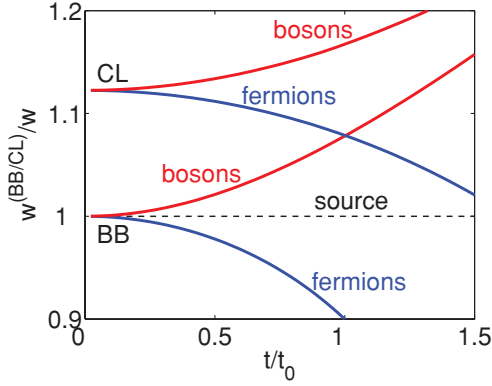


FIG. 8. (Color online) Widths (solid lines: bosons, red; fermions, blue) of the BB and CL pair correlations, $w^{(\text{BB})}$ and $w^{(\text{CL})}$, relative to the width of the source condensate as a function of time, for the molecular BEC profile (1) of Fig. 1.

from a higher asymptotic value, $w^{(\text{CL})} \simeq 1.12w$, than the BB width. The short-time asymptotic behavior is in agreement with the analytic results obtained in Sec. V.

For longer durations of dissociation—while still within the range of validity of the undepleted molecular-field approximation—we see that the BB correlation width grows faster (for bosons) than the CL correlation width, indicating the possibility that it may eventually become broader than the CL width. A similar behavior has been recently found in first-principle simulations of a related system of atomic four-wave mixing via condensate collisions [46]. Moreover, it has been shown that in the long-time limit the BB correlation width indeed becomes broader than the CL correlation, in agreement with the experimental measurements of Ref. [34].

For comparison, we have also performed an analysis of the dynamics of the BB and CL correlation widths for a Gaussian density profile of the source molecular BEC. The numerical results are in good agreement with the analytic results presented in Sec. VB.

D. Relative number squeezing

As an alternative measure of the strength of atom-atom correlations, we now calculate the variance of relative atom number fluctuations for atoms in different spin states and with equal but opposite momenta $\pm k_0$,

$$V_{k_0, -k_0}(t) = \langle [\Delta(\hat{n}_{1, k_0} - \hat{n}_{2, -k_0})]^2 \rangle / \Delta_{\text{SN}}, \quad (23)$$

where Δ_{SN} is the shot-noise level that originates from uncorrelated states. The atom number operators are defined by $\hat{n}_{j, \pm k_0}(t) = \int_K dk \hat{n}_j(k, t)$ [with $\hat{n}_j(k, t) = \hat{a}_j^\dagger(k, t) \hat{a}_j(k, t)$], where K is the counting length around $\pm k_0$. On a computational lattice the simplest choice of K that does not require explicit binning of the signal is $K = \Delta k$, where Δk is the lattice spacing, and therefore $\hat{n}_{j, \pm k_0}(t) = \hat{n}_j(\pm k_0, t) \Delta k$.

The shot-noise level Δ_{SN} is different for bosons and fermions. For the bosonic case, Δ_{SN} is given by the sum of variances of the individual mode occupancies with Poissonian statistics (as in the coherent state), implying that $\Delta_{\text{SN}} = \langle \hat{n}_{1, k_0} \rangle + \langle \hat{n}_{2, -k_0} \rangle$. For the fermionic case, the sum of the variances of two uncorrelated modes is $\Delta_{\text{SN}} = \langle \hat{n}_{1, k_0} \rangle (1 - \langle \hat{n}_{1, k_0} \rangle) + \langle \hat{n}_{2, -k_0} \rangle (1 - \langle \hat{n}_{2, -k_0} \rangle)$ [36], which is independent of the states of individual modes. The relative number variance (23) in both cases can be combined into the following expression:

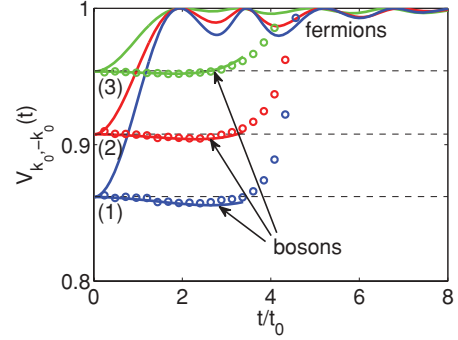


FIG. 9. (Color online) Relative number variance for dissociation into fermionic and bosonic atom pairs (full curves) within the undepleted molecular approximation. The dashed horizontal lines are the analytic results in the short-time asymptotic limit [Eq. (40)] from Sec. V. The three different sets of curves correspond to three different molecular BEC profiles of Fig. 1. The circles are from the exact positive- P simulations for bosons that take into account the molecular depletion.

where $s = 0$ and $s = 1$ for bosons and for fermions, respectively, and we have taken into account that $\langle \hat{n}_{1, k_0} \rangle = \langle \hat{n}_{2, -k_0} \rangle$ and $g_{11}^{(2)}(k_0, k_0, t) = g_{22}^{(2)}(-k_0, -k_0, t)$. Note that $g_{11}^{(2)}(k_0, k_0, t) = 0$ in the fermionic case due to the Pauli exclusion principle. Variance $V_{k_0, -k_0}(t) < 1$ implies squeezing of relative number fluctuations below the shot-noise level.

In Fig. 9 we plot the relative number variance for dissociation into fermionic (solid oscillatory curves) and bosonic (solid curves that initially follow the dashed horizontal lines) atom pairs for the three different sizes of the molecular BEC density profile of Fig. 1. The horizontal dashed lines are the respective analytic results (see Sec. V) in the short-time limit showing a common asymptotic behavior for bosons and fermions in the limit $t \rightarrow 0$. In this limit the atomic mode populations are much smaller than 1 and the quantum statistical effects do not show up. The numerical results for bosonic atoms are stopped around $t/t_0 \sim 3.5$; at this time the total number of atoms produced corresponds to more than 10% conversion and the undepleted molecular approximation is no longer valid. For the fermionic atoms the converted fraction remains less than 10% for the entire time window plotted. The circles that follow the bosonic solid curves for up to $t/t_0 \sim 3.5$ are from the exact positive- P method (see Sec. VI) and demonstrate the validity of the undepleted molecular approximation within this time window.

We see that both bosonic and fermionic cases display relative number squeezing that depends strongly on the size of the molecular BEC. The larger the molecular BEC is, the stronger is the relative number squeezing, implying that the degrading role of mode-mixing due to the source inhomogeneity

is a weaker effect when the molecular BEC density profile is closer to uniform. The reduction of squeezing and the nontrivial oscillatory behavior in the fermionic cases reflect the oscillatory behavior of the fermionic mode populations and the anomalous density $|m_{12}(k_0, -k_0, t)|$, as explained in the discussion of the oscillations in the BB peak correlation in Fig. 6; at time instances when the populations become close to 0 or 1, the fermionic shot-noise itself becomes vanishingly small and therefore the degree of squeezing below the shot-noise level diminishes [36].

In all three examples of Fig. 9 the lattice spacing is chosen as $\Delta k = 1875 \simeq \pi/2R_{\text{TF}}^{(3)} \text{ m}^{-1}$, where $R_{\text{TF}}^{(3)}$ is the TF radius of the molecular BEC profile (3) of Fig. 1. This is the largest spacing that is capable of resolving the relevant details and correlation lengths in momentum space for all three cases, and we see that the degree of squeezing is not particularly large in all examples. The strongest squeezing is for the case of the largest molecular BEC [curve (1)] and is only $\sim 14\%$ at short times.

This relatively modest degrees of squeezing in the examples of Fig. 9 can be contrasted to the ideal situation of 100% squeezing achievable in a completely uniform system that permits analytic solution in the undepleted molecular approximation [36]. The strong departure in the actual degree of squeezing from the prediction of the idealized uniform model is perhaps the strongest manifestation of the role of mode-mixing in realistic inhomogeneous systems. As shown previously [40,49], squeezing can be enhanced by binning the atomic signal into bins of larger size, in which case Eq. (24) is no longer applicable.

V. ANALYTIC TREATMENT IN THE SHORT-TIME LIMIT

In this section we present the results of an analytic treatment of the problem of molecular dissociation in the short-time limit in 1D, 2D, and 3D. Our approach is based on perturbative expansion in time, starting with the operator equations of motion in the undepleted molecular-field approximation [Eq. (4)]. Even though the present results are applicable for even shorter time scales than those of the numerical treatment of the previous section, their analytic transparency provides useful insights into the problem of atom-atom correlations as it has recently been demonstrated for a closely related problem of atomic four-wave mixing via condensate collisions [46]. For molecular dissociation, the present analytic approach in nonuniform 1D systems has been employed in Ref. [48]; here we present the details of derivations and extend the results to 2D and 3D systems.

The short-time perturbative treatment is based on the Taylor expansion in time, up to terms of order t^2 ,

$$\hat{a}_j(\mathbf{k}, t) = \hat{a}_j(\mathbf{k}, 0) + t \left. \frac{\partial \hat{a}_j(\mathbf{k}, t)}{\partial t} \right|_{t=0} + \frac{t^2}{2} \left. \frac{\partial^2 \hat{a}_j(\mathbf{k}, t)}{\partial t^2} \right|_{t=0} + \dots, \quad (25)$$

which is valid for $t \ll t_0$, where $t_0 \equiv 1/\chi\sqrt{\rho_0}$ is the characteristic time scale. We recall that, in the definition of t_0 for 1D, 2D, and 3D systems, the coupling constant χ and the molecular BEC peak density ρ_0 are to be understood as their 1D, 2D, and 3D counterparts (see, e.g., [44]), but we

suppress the respective indices for simplicity. In all cases, the units of χ and ρ_0 are such that $1/\chi\sqrt{\rho_0}$ has units of time. With the preceding expansion, one can check that the commutation (for bosons) and anticommutation (for fermions) relations for the creation and annihilation operators are given by $[\hat{a}_i(\mathbf{k}, t), \hat{a}_j^\dagger(\mathbf{k}', t)]_{\mp} \simeq \delta_{ij}\delta(\mathbf{k} - \mathbf{k}')$, up to terms of the order of t^2 .

Using the right-hand sides of the generating equations of motion (4) for calculating the derivative terms in Eq. (25), we obtain the following expressions for the anomalous and normal densities in the lowest order in t , in $D = 1, 2$, and 3 dimensions:

$$\begin{aligned} |m_{12}(\mathbf{k}, \mathbf{k}', t)| &= |\langle \hat{a}_1(\mathbf{k}, t) \hat{a}_2(\mathbf{k}', t) \rangle| \\ &\simeq \frac{t}{(2\pi)^{D/2}} |\tilde{g}(\mathbf{k} + \mathbf{k}')| \\ &= \frac{t}{(2\pi)^D} \left| \int d^D \mathbf{x} e^{i(\mathbf{k} + \mathbf{k}') \cdot \mathbf{x}} g(\mathbf{x}) \right|, \quad (26) \end{aligned}$$

$$\begin{aligned} n_j(\mathbf{k}, \mathbf{k}', t) &= \langle \hat{a}_j^\dagger(\mathbf{k}, t) \hat{a}_j(\mathbf{k}', t) \rangle \\ &\simeq \frac{t^2}{(2\pi)^D} \int d^D \mathbf{q} \tilde{g}^*(\mathbf{q} + \mathbf{k}) \tilde{g}(\mathbf{q} + \mathbf{k}') \\ &= \frac{t^2}{(2\pi)^D} \int d^D \mathbf{x} e^{i(\mathbf{k} - \mathbf{k}') \cdot \mathbf{x}} |g(\mathbf{x})|^2. \quad (27) \end{aligned}$$

Recalling Eqs. (20) and (21) and viewing Eqs. (26) and (27) in the context of BB and CL correlation functions, we see that the width of the CL correlation between the same-spin atoms [Eq. (21)] is determined by the square of the Fourier transform of the square of the effective coupling $g(\mathbf{x})$. The width of the BB correlation [Eq. (20)] between the different spin-state atoms, on the other hand, is determined by the square of the Fourier transform of $g(\mathbf{x})$. Since the function $g(\mathbf{x})^2$ is narrower than $g(\mathbf{x})$ and the converse is true for their respective Fourier transforms, we immediately deduce that the CL momentum correlation is generally broader than the BB correlation. These conclusions are true for any shape of the source condensate and apply to both bosonic and fermionic statistics in the short-time limit.

A. Thomas-Fermi parabolic density profiles

In this subsection we consider specific density profiles of the molecular BEC and use the perturbative results of Eqs. (26) and (27) for calculating atom-atom pair correlations and the relative number squeezing in the short-time limit. As one of the most typical situations, we start with a parabolic density profile characteristic of an interacting BEC in a harmonic trap in the TF limit.

1. One dimension (1D)

In 1D we assume that the molecular BEC profile is given by an inverted TF parabola, $\rho_0(x) = \rho_0(1 - x^2/R_{\text{TF}}^2)$ for $x < R_{\text{TF}}$ [and $\rho_0(x) = 0$ for $x \geq R_{\text{TF}}$], where $\rho_0 \equiv \rho_0(0)$ is the peak density. Accordingly, the effective coupling constant is given by $g(x) = \chi\sqrt{\rho_0}(1 - x^2/R_{\text{TF}}^2)^{1/2}$. The integrals appearing in

Eqs. (26) and (27) can be expressed in terms of Bessel functions, using the following integral representation [73]:

$$J_\nu(q) = \frac{2(q/2)^\nu}{\sqrt{\pi}\Gamma(\nu+1/2)} \int_0^1 d\xi (1-\xi^2)^{\nu-1/2} \cos(q\xi), \quad (28)$$

where $\nu > -1/2$ and $\Gamma(\nu)$ is the γ function. Accordingly, the integrals in Eqs. (26) and (27) yield

$$|m_{12}(k, k', t)| \simeq \frac{t\chi\sqrt{\rho_0}R_{\text{TF}}}{2} \frac{J_1[(k+k')R_{\text{TF}}]}{(k+k')R_{\text{TF}}}, \quad (29)$$

$$n_j(k, k', t) \simeq \frac{\sqrt{2}t^2\chi^2\rho_0R_{\text{TF}}}{\sqrt{\pi}} \frac{J_{3/2}[(k-k')R_{\text{TF}}]}{[(k-k')R_{\text{TF}}]^{3/2}}. \quad (30)$$

Substitution of these expressions into Eqs. (20) and (21) leads to the following results for the BB and CL pair correlation functions:

$$g_{12}^{(2)}(k, k', t) \simeq 1 + \frac{9\pi^2}{16t^2\chi^2\rho_0} \frac{\{J_1[(k+k')R_{\text{TF}}]\}^2}{[(k+k')R_{\text{TF}}]^2}, \quad (31)$$

$$g_{jj}^{(2)}(k, k', t) \simeq 1 \pm \frac{9\pi}{2} \frac{\{J_{3/2}[(k-k')R_{\text{TF}}]\}^2}{[(k-k')R_{\text{TF}}]^3}. \quad (32)$$

These results are valid for $t \ll t_0$, and are plotted in Fig. 10 as a function of k , for $k' = k_0$ and $t = 0.1t_0$. Once scaled with respect to the corresponding peak values and plotted as in Fig. 7, the curves in Fig. 10 follow closely the bosonic and fermionic numerical results shown in Fig. 7. Interestingly, even beyond the strict range of applicability of the analytic results of Eqs. (31) and (32), they show good agreement with the numerical results of the previous section, valid for up to $t \sim t_0$. For example, at $t = t_0$ the differences between the BB and CL correlation widths, evaluated using the analytic and numerical results, are less than 10%.

The correlation widths that follow from Eqs. (20) and (21) are

$$w^{(\text{BB})} = w \simeq 1.62/R_{\text{TF}}, \quad (33)$$

$$w^{(\text{CL})} \simeq 1.12w \simeq 1.81/R_{\text{TF}}, \quad (34)$$

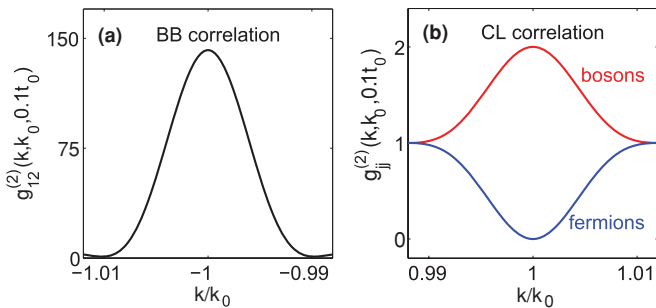


FIG. 10. (Color online) Analytic results of Eqs. (31) and (32) for the atom-atom pair correlation functions at $t = 0.1t_0$, for the case of a TF parabolic profile of the molecular BEC with $R_{\text{TF}} = 250 \mu\text{m}$. Other parameters are as in Fig. 2. (a) $g_{12}^{(2)}(k, k_0, 0.1t_0)$ as a function of k for fermionic and bosonic atom pairs in two different spin states, showing the back-to-back correlation peak at $k = -k_0$. (b) Pair correlation for the same-spin atoms $g_{jj}^{(2)}(k, k_0, t)$ in dissociation into distinguishable (fermionic or bosonic) atom pairs, showing a CL HBT peak for bosons or a HBT dip for fermions at $k = k_0$.

and therefore $w^{(\text{CL})}/w^{(\text{BB})} \simeq 1.12$. Here $w \simeq 1.62/R_{\text{TF}}$ is the width of the molecular BEC momentum distribution, $n_0(k) = |\int dx \sqrt{\rho_0(x)} \exp(-ikx)/(2\pi)^{1/2}|^2$, given by

$$n_0(k) = \frac{\pi\rho_0}{2} \frac{[J_1(kR_{\text{TF}})]^2}{k^2}. \quad (35)$$

Inverting the relationship between the second- and first-order correlation functions, $|g_{jj}^{(1)}(k, k', t)| = \sqrt{|g_{jj}^{(2)}(k, k', t) - 1|}$, we can also find the width of the first-order correlation function, $\Delta k^{(\text{coh})}$, which gives the phase coherence length and defines the size of an atomic mode in free space. From the preceding analytic result for $g_{jj}^{(2)}(k, k', t)$, we find that the first-order coherence length in the short-time limit is approximately $\Delta k^{(\text{coh})} = 2.50/R_{\text{TF}}$. In terms of the momentum width of the source condensate w , this corresponds to $\Delta k^{(\text{coh})} = 1.54w$, and shows that the first-order coherence length is larger than the second-order correlation length $w^{(\text{CL})}$.

Using the asymptotic behavior of the Bessel function, $J_\nu(z) \simeq (z/2)^\nu/\Gamma(\nu+1)$ for $z \ll 1$ ($\nu \neq -1, -2, \dots$), Eqs. (29) and (30) at $k' = \mp k$ give, respectively, the peak value of the anomalous density $m_{12}(k, t) \equiv m_{12}(k, -k, t)$ and the atomic momentum distribution in the spin state j , $n_j(k, t) \equiv n_j(k, k, t)$:

$$|m_{12}(k, t)| \simeq \frac{t\chi\sqrt{\rho_0}R_{\text{TF}}}{4}, \quad (36)$$

$$n_j(k, t) \simeq \frac{2t^2\chi^2\rho_0R_{\text{TF}}}{3\pi}. \quad (37)$$

The peak densities are uniform in the short-time limit, corresponding to *spontaneous* initiation of dissociation, which populates the atomic modes uniformly without the need to strictly conserve energy. A double-peaked structure with maxima around $|k| = \pm k_0$ (which in 2D and 3D turns into a circle and a sphere of radius $|\mathbf{k}| = k_0$ [36,39]) forms later in time [17], when the present analytic results are not applicable.

Similarly, we can find that the peak values of the pair correlation functions (31) and (32) are given by

$$g_{12}^{(2)}(k, -k, t) \simeq 1 + \frac{9\pi^2}{64t^2\chi^2\rho_0}, \quad (38)$$

$$g_{jj}^{(2)}(k, k, t) = \begin{cases} 2, & \text{bosons,} \\ 0, & \text{fermions.} \end{cases} \quad (39)$$

The inverse square dependence of the BB correlation peak, $g_{12}^{(2)}(k, -k, t)$, on time (for $t \ll t_0$) is in good agreement with the numerical results of the undepleted molecular-field approximation, as well as with the results of first-principles simulations using the positive- P method (see Fig. 6). The peak values of the CL correlation, $g_{jj}^{(2)}(k, k, t)$, correspond to the expected HBT bunching for bosons and the HBT dip for fermions.

Finally, we calculate the short-time asymptote for the relative number variance [Eq. (24)] and find the following simple result:

$$V_{k_0, -k_0}(t) \simeq 1 - \frac{3\pi \Delta k R_{\text{TF}}}{32}. \quad (40)$$

In this limit the atomic mode populations are much smaller than 1, bosonic and fermionic shot noises are approximately equal to each other, and we do not see any difference in the relative number squeezing for bosons and fermions. In Fig. 9, the results of Eq. (40) for three different sizes of the initial molecular BEC are shown as horizontal dashed lines. As we see, the relative number squeezing at short times depends merely on the size of the source condensate R_{TF} and the size of the counting cell Δk . The small geometric prefactor in the second term is determined by the shape of the source condensate (TF parabola in the present case). Together with the resolution requirement of $\Delta k \lesssim 1/R_{\text{TF}}$, the smallness of this prefactor ensures that $V_{k_0, -k_0}(t) > 0$; at the same time this implies that the raw (unbinned) squeezing can be very weak for small R_{TF} .

2. Two dimensions (2D)

In 2D, the TF density profile of the molecular BEC in a harmonic trap is given by $\rho_0(\mathbf{x}) = \rho_0(1 - x^2/R_{\text{TF},x}^2 - y^2/R_{\text{TF},y}^2)$ for $x^2/R_{\text{TF},x}^2 + y^2/R_{\text{TF},y}^2 < 1$ [and $\rho_0(\mathbf{x}) = 0$ otherwise], and therefore $g(\mathbf{x}) = \chi\sqrt{\rho_0}(1 - x^2/R_{\text{TF},x}^2 - y^2/R_{\text{TF},y}^2)^{1/2}$. The analysis of the short-time asymptotic behavior of the correlation functions is essentially the same as in 1D, except that one has to specify in advance the direction of the displacement $\Delta\mathbf{k}$ between the pair of momentum vectors \mathbf{k} and \mathbf{k}' for which the correlations are being analyzed. For definiteness, we consider BB and CL correlations for which the displacement $\Delta\mathbf{k}$ is along one of the Cartesian coordinates, k_i ($i = x, y$). In other words, we consider correlations between \mathbf{k} and $\mathbf{k}' = \pm\mathbf{k} + \mathbf{e}_i\Delta k_i$, where \mathbf{e}_i is the unit vector in the k_i direction; the plus sign is for the CL correlation, and the minus sign is for the BB correlation. In the results that follow, the dependence on \mathbf{k} is absent and we omit it for notational simplicity.

The 2D integrals in Eqs. (26) and (27) can again be performed in terms of Bessel functions (see Appendix A), and we obtain

$$|m_{12}(k_i, k'_i, t)| \simeq \frac{t\chi\sqrt{\rho_0}\overline{R_{\text{TF}}}^2}{2\sqrt{2\pi}} \frac{J_{3/2}[(k_i + k'_i)R_{\text{TF},i}]}{[(k_i + k'_i)R_{\text{TF},i}]^{3/2}}, \quad (41)$$

$$n_j(k_i, k'_i, t) \simeq \frac{t^2\chi^2\rho_0\overline{R_{\text{TF}}}^2}{\pi} \frac{J_2[(k_i - k'_i)R_{\text{TF},i}]}{[(k_i - k'_i)R_{\text{TF},i}]^2}, \quad (42)$$

where $\overline{R_{\text{TF}}} = (R_{\text{TF},x}R_{\text{TF},y})^{1/2}$ is the geometric mean TF radius. The preceding expressions lead to the following explicit results for the second-order correlation functions:

$$g_{12}^{(2)}(k_i, k'_i, t) \simeq 1 + \frac{8\pi}{t^2\chi^2\rho_0} \frac{\{J_{3/2}[(k_i + k'_i)R_{\text{TF},i}]\}^2}{[(k_i + k'_i)R_{\text{TF},i}]^3}, \quad (43)$$

$$g_{jj}^{(2)}(k_i, k'_i, t) \simeq 1 \pm \frac{64\{J_2[(k_i - k'_i)R_{\text{TF},i}]\}^2}{[(k_i - k'_i)R_{\text{TF},i}]^4}. \quad (44)$$

The dependence of $g_{12}^{(2)}(k_i, k'_i, t)$ on $k_i + k'_i$ and its peak at $k_i + k'_i = 0$ implies that it describes the BB correlation of different spin atoms with equal but opposite momenta, for which $\mathbf{k}' \simeq -\mathbf{k}$ and is offset from $-\mathbf{k}$ by an amount Δk_i in the i th direction. Similarly, the dependence of $g_{jj}^{(2)}(k_i, k'_i, t)$ on $k_i - k'_i$ and its peak at $k_i - k'_i = 0$ corresponds to the CL correlation between pairs of atoms in the same spin state, for which $\mathbf{k}' \simeq \mathbf{k}$ and is offset by an amount Δk_i . The qualitative

behavior of the BB and CL correlation functions is the same as in 1D (Fig. 10) whereas the quantitative differences enter through the width of the correlations and their respective peak values.

The widths of the BB and CL correlation functions in 2D are

$$w_i^{(\text{BB})} = w_i \simeq 1.81/R_{\text{TF},i}, \quad (45)$$

$$w_i^{(\text{CL})} \simeq 1.10w_i \simeq 1.99/R_{\text{TF},i}, \quad (46)$$

and therefore $w_i^{(\text{CL})}/w_i^{(\text{BB})} \simeq 1.10$. Relative to the source width w_i , the CL correlation width in 2D is narrower than in 1D, while the BB correlation width is equal to w_i . Here, $w_i \simeq 1.81/R_{\text{TF},i}$ is the width of the momentum distribution of the molecular BEC along i , found from $n_0(k_i) = |\int d^2\mathbf{x}\sqrt{\rho_0(\mathbf{x})}\exp(-ik_ix_i)/(2\pi)|^2$ (see Appendix A) as

$$n_0(k_i) = \frac{\pi\rho_0\overline{R_{\text{TF}}}^4}{2} \frac{[J_{3/2}(k_iR_{\text{TF},i})]^2}{(k_iR_{\text{TF},i})^3}. \quad (47)$$

The first-order coherence length in 2D, which follows from $|g_{jj}^{(1)}(k_i, k'_i, t)| = \sqrt{|g_{jj}^{(2)}(k_i, k'_i, t) - 1|}$, is given by $\Delta k_i^{(\text{coh})} \simeq 2.75/R_{\text{TF},i}$ and therefore $\Delta k_i^{(\text{coh})} \simeq 1.52w_i$.

The peak values of the anomalous and normal densities, $m_{12}(\mathbf{k}, t) \equiv m_{12}(\mathbf{k}, -\mathbf{k}, t)$ and $n_j(\mathbf{k}, t) \equiv n_j(\mathbf{k}, \mathbf{k}, t)$, are given by

$$m_{12}(\mathbf{k}, t) \simeq \frac{t\chi\sqrt{\rho_0}\overline{R_{\text{TF}}}^2}{6\pi}, \quad (48)$$

$$n_j(\mathbf{k}, t) \simeq \frac{t^2\chi^2\rho_0\overline{R_{\text{TF}}}^2}{8\pi}. \quad (49)$$

The peak CL correlation function $g_{jj}^{(2)}(\mathbf{k}, \mathbf{k}, t)$ is the same as in Eq. (39), whereas the peak BB correlation is given by

$$g_{12}^{(2)}(\mathbf{k}, -\mathbf{k}, t) \simeq 1 + \frac{16}{9t^2\chi^2\rho_0}. \quad (50)$$

This result is qualitatively similar to the 1D result of Eq. (38), except that the numerical prefactor in the second term is different. The same is true for the relative number variance. In 2D it is given by

$$V_{\mathbf{k}_0, -\mathbf{k}_0}(t) \simeq 1 - \frac{2(\overline{\Delta k})^2(\overline{R_{\text{TF}}})^2}{9\pi}, \quad (51)$$

where $\overline{\Delta k} = (\Delta k_x\Delta k_y)^{1/2}$ is the geometric mean lattice spacing, with $\overline{\Delta k}^2$ giving the counting area. Comparing this result with $V_{k_0, -k_0}(t)$ in 1D [Eq. (40)], we see that the raw squeezing is weaker in 2D than in 1D, for the same size of the molecular BEC and the same lattice spacing.

3. Three dimensions (3D)

In 3D the TF density profile is given by $\rho_0(\mathbf{x}) = \rho_0(1 - x^2/R_{\text{TF},x}^2 - y^2/R_{\text{TF},y}^2 - z^2/R_{\text{TF},z}^2)$ for $x^2/R_{\text{TF},x}^2 + y^2/R_{\text{TF},y}^2 + z^2/R_{\text{TF},z}^2 < 1$ [and $\rho_0(\mathbf{x}) = 0$ otherwise], and therefore $g(\mathbf{x}) = \chi\sqrt{\rho_0}(1 - x^2/R_{\text{TF},x}^2 - y^2/R_{\text{TF},y}^2 - z^2/R_{\text{TF},z}^2)^{1/2}$. As in 2D, we are interested in BB and CL density correlations between two momentum components at \mathbf{k} and \mathbf{k}' , for which the displacement $\Delta\mathbf{k} = \mathbf{k} - \mathbf{k}'$ is along one of the Cartesian coordinates, k_i , where $i = x, y, z$. The 3D integrals in Eqs. (26)

and (27) can again be performed in terms of Bessel functions (see Appendix B), and we obtain

$$|m_{12}(k_i, k'_i, t)| \simeq \frac{t\chi\sqrt{\rho_0}\overline{R_{\text{TF}}}^3}{4\pi} \frac{J_2[(k_i + k'_i)R_{\text{TF},i}]}{[(k_i + k'_i)R_{\text{TF},i}]^2}, \quad (52)$$

$$n_j(k_i, k'_i, t) \simeq \frac{t^2\chi^2\rho_0\overline{R_{\text{TF}}}^3}{\pi\sqrt{2\pi}} \frac{J_{5/2}[(k_i - k'_i)R_{\text{TF},i}]}{[(k_i - k'_i)R_{\text{TF},i}]^{5/2}}, \quad (53)$$

where $\overline{R_{\text{TF}}} = (R_{\text{TF},x}R_{\text{TF},y}R_{\text{TF},z})^{1/3}$ is the geometric mean TF radius. The BB and CL correlations following from these expressions are

$$g_{12}^{(2)}(k_i, k'_i, t) \simeq 1 + \frac{225\pi^2}{16t^2\chi^2\rho_0} \frac{\{J_2[(k_i + k'_i)R_{\text{TF},i}]\}^2}{[(k_i + k'_i)R_{\text{TF},i}]^4}, \quad (54)$$

$$g_{jj}^{(2)}(k_i, k'_i, t) \simeq 1 \pm \frac{225\pi}{2} \frac{\{J_{5/2}[(k_i - k'_i)R_{\text{TF},i}]\}^2}{[(k_i - k'_i)R_{\text{TF},i}]^5}. \quad (55)$$

As in 2D, the qualitative behavior of the BB and CL correlation functions is the same as in 1D (Fig. 10), whereas the quantitative differences enter through the width and the peak values.

The widths of the BB and CL correlations in 3D are given by

$$w_i^{(\text{BB})} = w_i \simeq 1.99/R_{\text{TF},i}, \quad (56)$$

$$w_i^{(\text{CL})} \simeq 1.08w_i \simeq 2.16/R_{\text{TF},i}, \quad (57)$$

and therefore $w_i^{(\text{CL})}/w_i^{(\text{BB})} \simeq 1.08$. The CL correlation width in 3D relative to the source width w_i is smaller than in 1D and 2D, whereas the relative BB correlation width is the same. Here $w_i \simeq 1.99/R_{\text{TF},i}$ is the width of the momentum distribution of the molecular BEC along i , found from $n_0(k_i) = |\int d^3\mathbf{x}\sqrt{\rho_0(\mathbf{x})}\exp(-ik_ix_i)/(2\pi)^{3/2}|^2$ (see Appendix B) as

$$n_0(k_i) = \frac{\pi\rho_0\overline{R_{\text{TF}}}^6}{2} \frac{[J_2(k_iR_{\text{TF},i})]^2}{(k_iR_{\text{TF},i})^4}. \quad (58)$$

The first-order coherence length in 3D, following from $|g_{jj}^{(1)}(k_i, k'_i, t)| = \sqrt{|g_{jj}^{(2)}(k_i, k'_i, t) - 1|}$, is given by $\Delta k_i^{(\text{coh})} \simeq 2.99/R_{\text{TF},i}$ and therefore $\Delta k_i^{(\text{coh})} \simeq 1.50w_i$. This is again larger than the second-order CL correlation width $w_i^{(\text{CL})} \simeq 1.08w_i$.

The peak values of the anomalous and normal densities in 3D are given by

$$n_j(\mathbf{k}, t) \simeq \frac{t^2\chi^2\rho_0\overline{R_{\text{TF}}}^3}{15\pi^2}, \quad (59)$$

$$m_{12}(\mathbf{k}, t) \simeq \frac{t\chi\sqrt{\rho_0}\overline{R_{\text{TF}}}^3}{32\pi}, \quad (60)$$

whereas the peak BB correlation is

$$g_{12}^{(2)}(\mathbf{k}, -\mathbf{k}, t) \simeq 1 + \frac{15^2\pi^2}{32^2t^2\chi^2\rho_0}. \quad (61)$$

The peak CL correlation function $g_{jj}^{(2)}(\mathbf{k}, \mathbf{k}, t)$ is the same as in Eq. (39). The result for $g_{12}^{(2)}(\mathbf{k}, -\mathbf{k}, t)$ is qualitatively similar to the 1D and 2D results of Eqs. (38) and (50), except that the numerical prefactor in the second term is different.

Finally, the relative number squeezing in 3D is determined by

$$V_{\mathbf{k}_0, -\mathbf{k}_0}(t) \simeq 1 - \frac{15(\overline{\Delta k})^3(\overline{R_{\text{TF}}})^3}{32^2}, \quad (62)$$

where $\overline{\Delta k} = (\Delta k_x\Delta k_y\Delta k_z)^{1/3}$ is the geometric mean lattice spacing, with $\overline{\Delta k}^3$ giving the counting volume. The raw squeezing in 3D is weaker than in 1D and 2D, for the same size of the molecular BEC and the same lattice spacing.

B. Gaussian density profiles

In this subsection we present the short-time analytic results for the correlation functions in the case of a Gaussian density profile of the source molecular BEC, $\rho_0(\mathbf{x}) = \rho_0 \exp(-\sum_{i=1}^D x_i^2/2S_i^2)$, where ρ_0 is the peak density and S_i is the rms width in the i th direction. The results for 1D, 2D, and 3D systems can be combined through setting $D = 1, 2$, or 3 . As in the case of the TF density profile, we are interested in BB and CL density correlations between two momentum components at \mathbf{k} and \mathbf{k}' , for which the displacement $\Delta\mathbf{k} = \mathbf{k} - \mathbf{k}'$ is along one of the Cartesian coordinates, k_i , where $i = x, y, z$ in 3D (in 2D, $i = x, y$, while in 1D, $i = x$). We define the momentum width of the molecular condensate along k_i via σ_i , which corresponds to the rms width $\sigma_i = 1/2S_i$ of a Gaussian

$$n_0(k_i) = \frac{\rho_0}{2^D(\overline{\sigma})^{2D}} \exp(-k_i^2/2\sigma_i^2), \quad (63)$$

where $n_0(k_i)$ is defined according to $n_0(k_i) = |\int d^D\mathbf{x}\sqrt{\rho_0(\mathbf{x})}\exp(-ik_ix_i)/(2\pi)^{D/2}|^2$ and $\overline{\sigma} = (\prod_{i=1}^D \sigma_i)^{1/D}$ is the geometric mean width.

With these definitions, the integrals in Eqs. (26) and (27), with $g(\mathbf{x}) = \chi\sqrt{\rho_0(\mathbf{x})}$, give

$$|m_{12}(k_i, k'_i, t)| \simeq \frac{t\chi\sqrt{\rho_0}}{2^D\pi^{D/2}\overline{\sigma}} \exp[-(k_i + k'_i)^2/4\sigma_i^2], \quad (64)$$

$$n_j(k_i, k'_i, t) \simeq \frac{t^2\chi^2\rho_0}{2^{D+D/2}\pi^{D/2}\overline{\sigma}} \exp[-(k_i - k'_i)^2/8\sigma_i^2], \quad (65)$$

and therefore the BB and CL correlation functions are

$$g_{12}^{(2)}(k, k', t) \simeq 1 + \frac{2^D}{t^2\chi^2\rho_0} \exp[-(k_i + k'_i)^2/2\sigma_i^2], \quad (66)$$

$$g_{jj}^{(2)}(k_i, k'_i, t) \simeq 1 \pm \exp[-(k_i - k'_i)^2/4\sigma_i^2]. \quad (67)$$

The BB and CL correlation widths are

$$\sigma^{(\text{BB})} = \sigma_i = 1/2S_i, \quad (68)$$

$$\sigma^{(\text{CL})} = \sqrt{2}\sigma_i = 1/\sqrt{2}S_i. \quad (69)$$

The CL correlation width, relative to the source width σ_i , in the present Gaussian case is broader than in the case of a TF parabolic density profile of the source molecular BEC, whereas the BB correlation width is equal to the width of the source as before.

The relative number squeezing is given by

$$V_{\mathbf{k}_0, -\mathbf{k}_0}(t) \simeq 1 - \left(\frac{2}{\pi}\right)^{D/2} \frac{(\overline{\Delta k})^D(\overline{S})^D}{(\overline{\sigma})^D}, \quad (70)$$

where $\bar{S} = (\prod_{i=1}^D S_i)^{1/D}$ is the geometric mean width of the molecular BEC in coordinate space and $\bar{\Delta k} = (\prod_{i=1}^D \Delta k_i)^{1/D}$. The general qualitative conclusions about relative number squeezing in 1D, 2D, and 3D remain the same as for the TF parabolic density profile of the source molecular BEC.

VI. EFFECTS OF MOLECULAR DEPLETION AND COLLISIONAL INTERACTIONS

In this section we discuss the role of molecular depletion and s -wave scattering interactions. We treat these effects explicitly using two alternative phase-space representation techniques: first-principles simulations using the positive- P method [74] and a truncated Wigner approximation [75,76]. Owing to the fact that these phase-space methods are currently well established for bosonic fields (see, e.g., [39,40,42,46,47,77,78]), we restrict our study only to dissociation into bosonic atoms. Development of similar techniques for fermions is under way [41,43], but they are so far limited to treating homogeneous systems and therefore are not adopted yet to the present problem of dissociation of spatially inhomogeneous molecular condensates.

To understand the role molecular depletion by itself, we first treat the dissociation dynamics governed by the Hamiltonian (1) without the s -wave scattering interactions. Since most of our previous numerical and analytic examples were given for the case of distinguishable atoms (which has its fermionic counterpart), we examine the role of molecular depletion in the same examples.

In the second part of this section we analyze the role of collisional interactions between the atoms and molecules and restrict our study to the case of indistinguishable bosonic atoms. More specifically, we treat molecule-molecule, molecule-atom, and atom-atom s -wave scattering interactions described by the respective s -wave scattering lengths a_{00} , a_{01} , and a_{11} . Our treatment automatically incorporates molecular depletion since the molecular field in all cases is treated quantum mechanically, without invoking the mean-field approximation. The restriction to the case of indistinguishable atoms is motivated by the need to keep the parameter space manageable, while still giving us an overall quantitative understanding of the role of these collisional processes. For comparison, in the case of dissociation into distinguishable atoms, a generic treatment would have to incorporate six different types of intra- and interspecies scattering processes described by six (generally different, and yet unknown for most of the species) scattering lengths a_{ij} ($i, j = 0, 1, 2$), which is a challenging task and is beyond the scope of the present article.

A. Role of molecular depletion

To model the quantum dynamics of dissociation beyond the undepleted molecular-field approximation, we use a first-principles phase-space method based on the positive- P representation. In this method, each pair of the field operators $\hat{\Psi}_i(x, t)$ and $\hat{\Psi}_i^\dagger(x, t)$ ($i = 0, 1, 2$) in the Hamiltonian (1) in 1D is represented by two complex stochastic fields $\Psi_i(x, t)$ and $\tilde{\Psi}_i(x, t)$ whose dynamics is governed by a set of stochastic

differential equations,

$$\begin{aligned} \frac{\partial \Psi_0}{\partial t} &= i \frac{\hbar}{2m_0} \frac{\partial^2 \Psi_0}{\partial x^2} - \chi \Psi_1 \Psi_2, \\ \frac{\partial \Psi_1}{\partial t} &= i \left[\frac{\hbar}{2m_1} \frac{\partial^2}{\partial x^2} - \Delta \right] \Psi_1 + \chi \Psi_0 \tilde{\Psi}_2 + \sqrt{\chi \Psi_0} \xi_1, \\ \frac{\partial \Psi_2}{\partial t} &= i \left[\frac{\hbar}{2m_2} \frac{\partial^2}{\partial x^2} - \Delta \right] \Psi_2 + \chi \Psi_0 \tilde{\Psi}_1 + \sqrt{\chi \Psi_0} \xi_1^*, \\ \frac{\partial \tilde{\Psi}_0}{\partial t} &= -i \frac{\hbar}{2m_0} \frac{\partial^2 \tilde{\Psi}_0}{\partial x^2} - \chi \tilde{\Psi}_1 \tilde{\Psi}_2, \\ \frac{\partial \tilde{\Psi}_1}{\partial t} &= -i \left[\frac{\hbar}{2m_1} \frac{\partial^2}{\partial x^2} - \Delta \right] \tilde{\Psi}_1 + \chi \tilde{\Psi}_0 \Psi_2 + \sqrt{\chi \tilde{\Psi}_0} \xi_2, \\ \frac{\partial \tilde{\Psi}_2}{\partial t} &= -i \left[\frac{\hbar}{2m_1} \frac{\partial^2}{\partial x^2} - \Delta \right] \tilde{\Psi}_2 + \chi \tilde{\Psi}_0 \Psi_1 + \sqrt{\chi \tilde{\Psi}_0} \xi_2^*. \end{aligned} \quad (71)$$

Here $\xi_1 = (\zeta_1 + i\zeta_2)/\sqrt{2}$ and $\xi_2 = (\zeta_3 + i\zeta_4)/\sqrt{2}$ are the complex noise terms, with $\zeta_j(x, t)$ ($j = 1, 2, 3, 4$) being real independent Gaussian noises with zero mean, $\langle \zeta_j(x, t) \rangle = 0$, and the following nonzero correlations: $\langle \zeta_i(x, t) \zeta_j(x', t') \rangle = \delta_{ij} \delta(x - x') \delta(t - t')$. The stochastic fields $\Psi_i(x, t)$ and $\tilde{\Psi}_i(x, t)$ are independent of each other [$\tilde{\Psi}_i(x, t) \neq \Psi_i^*(x, t)$, $t > 0$], except in the mean, $\langle \tilde{\Psi}_i(x, t) \rangle = \langle \Psi_i^*(x, t) \rangle$, where the brackets refer to stochastic averages with respect to the positive- P distribution function. In numerical realizations, this is represented by an ensemble average over a large number of stochastic realizations (trajectories). Observables described by quantum mechanical ensemble averages over normally ordered operator products have an exact correspondence with stochastic averages over the fields $\Psi(x, t)$ and $\tilde{\Psi}(x, t)$.

The initial condition for our simulations is a vacuum state for the atomic fields and a coherent state for the molecular condensate, with $\tilde{\Psi}_0(x, 0) = \Psi_0^*(x, 0)$. In the numerical examples, we assume that the molecular condensates initially have the same density profiles as those used in our simulations within the undepleted molecular approximation (see Fig. 1). We note that in the undepleted case, these density profiles were assumed to originate from the ground-state solution of the GP equation in a harmonic trap, which in the TF limit gives inverted parabolas whose TF radii depend on the strength of molecule-molecule interactions. In the present case, we treat the molecular depletion but ignore the molecule-molecule s -wave scattering interactions; accordingly, the ground state of a harmonic trap would result in a Gaussian density profile rather than an inverted parabola. To make the present treatment self-consistent, yet directly comparable with the numerical examples analyzed in the undepleted case, we therefore assume that the same, near-parabolic initial density profiles are created by tailoring the shape of the trapping potential.

The results of the exact positive- P simulations are shown in Figs. 2, 6, and 9; the comparison with the results of the undepleted molecular approximation is discussed in the respective parts of text in Sec. IV. A known drawback of the positive- P method is that it suffers from increasingly large sampling errors due to the boundary terms problem [79,80] as the simulation time increases, eventually leading to diverging results. In the present examples without the s -wave scattering terms, the useful simulation times were limited to $t \simeq 6.5t_0$.

In order to go beyond the simulation durations achievable via the positive- P method, we have also performed simulations using the truncated Wigner-function approach. Unlike the positive- P method, it is an approximate approach as it involves neglecting or truncating third- and higher-order derivative terms in the evolution equation for the Wigner function. This is necessary in order to obtain an equation in the form of a Fokker-Planck equation which can then be mapped onto a set of stochastic differential equations. These equations formally render as deterministic mean-field (or GP-like) equations,

$$\begin{aligned} \frac{\partial \Psi_0}{\partial t} &= i \frac{\hbar}{2m_0} \frac{\partial^2 \Psi_0}{\partial x^2} - \chi \Psi_1 \Psi_2, \\ \frac{\partial \Psi_1}{\partial t} &= i \left[\frac{\hbar}{2m_1} \frac{\partial^2}{\partial x^2} - \Delta \right] \Psi_1 + \chi \Psi_0 \Psi_2^*, \\ \frac{\partial \Psi_2}{\partial t} &= i \left[\frac{\hbar}{2m_2} \frac{\partial^2}{\partial x^2} - \Delta \right] \Psi_2 + \chi \Psi_0 \Psi_1^*, \end{aligned} \quad (72)$$

however, their stochastic nature and quantum fluctuations are included by way of a noise contribution in the initial state for the molecular and atomic fields. The addition of this initial vacuum noise ensures that the initial states of Ψ_0 and $\Psi_{1,2}$ represent the Wigner function of an initial coherent-state BEC for the molecules and an initial vacuum state for the atoms, respectively. The corresponding stochastic averages with the Wigner distribution function correspond to symmetrically ordered operator products, so that the calculation of observables represented by normally ordered operator products needs appropriate symmetrization.

The results of our simulations using the Wigner function method are shown in Figs. 2 and 6 and are in excellent agreement with the exact positive- P results, thus reinforcing our confidence in the adequacy of this method for treating the problem of molecular dissociation.

B. Role of collisional interactions

We now turn to the treatment of s -wave scattering interactions in the case of dissociation into indistinguishable bosonic atoms. This case is described by the Hamiltonian (8), together with the additional quartic terms,

$$\hat{H}_{\text{int}} = \sum_{i,j=0,1} \frac{\hbar U_{ij}^{(1D)}}{2} \int dx \hat{\Psi}_i^\dagger \hat{\Psi}_j^\dagger \hat{\Psi}_j \hat{\Psi}_i. \quad (73)$$

Here $U_{00}^{(1D)}$, $U_{01}^{(1D)} = U_{10}^{(1D)}$, and $U_{11}^{(1D)}$ correspond to the effective 1D coupling constants describing, respectively, molecule-molecule, molecule-atom, and atom-atom interactions that are proportional to the 3D scattering lengths a_{00} , a_{01} , and a_{11} . In the case of a harmonic transverse confinement realizing a cigar-shaped 1D system, these constants are given by $U_{ii}^{(1D)} = 2\omega_\perp a_{ii}$ and $U_{01}^{(1D)} = (3/\sqrt{2})\omega_\perp a_{01}$, where ω_\perp is the transverse harmonic oscillator frequency [81].

The treatment of the s -wave scattering interactions using the positive- P method is a challenging task because the problem of growing sampling errors becomes more severe than before. The useful simulation time with realistic physical parameters reduces to sub-milliseconds in our examples, which is too short to give any new insights beyond the undepleted molecular approximation (see also Ref. [39]). As discussed in Ref. [42],

the most reliable method in this situation is the truncated Wigner approach, which produces stochastic equations that remain stable for much longer simulation durations than the positive- P equations. The Wigner equations in the present case are

$$\begin{aligned} \frac{\partial \Psi_0}{\partial t} &= i \frac{\hbar}{2m_0} \frac{\partial^2 \Psi_0}{\partial x^2} - i \sum_{j=0,1} U_{0j} |\Psi_j|^2 \Psi_0 - \frac{\chi}{2} \Psi_2^2, \\ \frac{\partial \Psi_1}{\partial t} &= i \left[\frac{\hbar}{2m_1} \frac{\partial^2}{\partial x^2} - \Delta - \sum_{j=0,1} U_{1j} |\Psi_j|^2 \right] \Psi_1 + \chi \Psi_0 \Psi_1^*, \end{aligned} \quad (74)$$

and the quantum fluctuations are introduced as previously via the noise contributions in the initial state for the molecular and atomic fields.

As an example relevant to practice, we treat $^{87}\text{Rb}_2$ molecules as in the experiments of Ref. [12] and use the 1D parameters described in [81]. In Fig. 11 we plot the total number of free dissociated atoms $N_1(t)$ relative to their initial number within the molecular condensate $2N_0(0)$. The two solid curves are reference examples, corresponding to

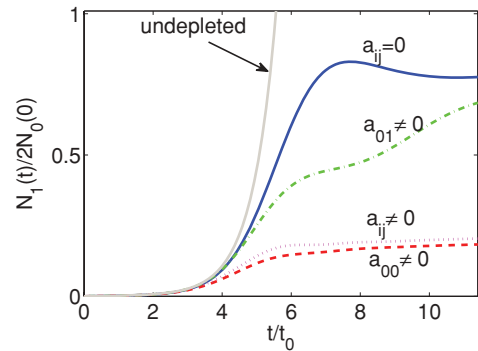


FIG. 11. (Color online) Fractional total atom number as a function of time, $N_1(t)/2N_0(0)$, in dissociation into indistinguishable bosonic atoms. The time scale $t_0 = 1/\chi\sqrt{\rho_0}$ in these examples is $t_0 \simeq 0.035$ s [81]. The two solid curves (light gray and blue) are reference examples, corresponding to the undepleted molecular approximation (labeled) and the case with molecular depletion but no s -wave scattering interactions ($a_{ij} = 0$ nm). The remaining three curves correspond to simulations in which we include: molecule-molecule interactions with $a_{00} = 3$ nm (and $a_{01} = a_{11} = 0$), dashed red curve; molecule-atom interactions with $a_{01} = 3$ nm (and $a_{00} = a_{11} = 0$), dash-dotted green curve; and all three s -wave scattering interactions with $a_{00} = a_{01} = a_{11} = 3$ nm, dotted magenta curve. In the undepleted case, we assume a near-parabolic initial density profile of the molecular BEC, with the peak 1D density $\rho_0 \simeq 1.8 \times 10^7$ m $^{-1}$ and a radius $R_{\text{TF}} \simeq 53$ μm in the TF limit (originating from a transverse trapping potential frequency of $\omega_\perp/2\pi = 54$ Hz and molecule-molecule 3D scattering length of $a_{00} = 3$ nm). In the cases with depletion but no s -wave scattering interactions, we assume a Gaussian density profile $\rho_0(x,0) = \rho_0 \exp(-x^2/2S_x^2)$ that has the same peak 1D density and an rms width of $S_x = 35$ μm which is chosen as to closely follow the near-parabolic profile for the interacting case in the central part of the cloud. The same near-parabolic initial density profile was used in the examples with $a_{00} = 3$ nm (dashed red and dotted magenta), and the same Gaussian profile was used in the example with $a_{01} = 3$ nm and $a_{00} = a_{11} = 0$ nm (dash-dotted green).

the undepleted molecular approximation (light gray) and the case when the molecular depletion is included, but all s -wave scattering interactions are still absent (blue curve). The dashed and the dash-dotted curves are, respectively, for the cases that include only molecule-molecule and molecule-atom interactions (the case with only atom-atom interactions was studied in [42]), while the dotted curve corresponds to the inclusion of all three types of s -wave scattering terms. As we see, all these curves agree with the curve for the undepleted molecular approximation for durations of $t/t_0 \lesssim 3$. We therefore conclude that the inclusion of s -wave scattering interactions reduces the regime of validity of the undepleted molecular approximation to durations corresponding approximately to 5% conversion, which is about twice lower than in the absence of these interactions.

In order to qualitatively understand the behavior of the different curves in Fig. 11, we note the following two dominant features: (1) the two curves (dashed red and dotted magenta) that correspond to having nonzero molecule-molecule interactions grow slower than the other curves, and (2) all curves with s -wave scattering interactions “bend” at around $t/t_0 \sim 5$ and do not reach the maximum conversion efficiency seen in the solid blue curve.

The slower growth of the curves that include the effect of molecule-molecule interactions is explained by the fact that the molecular condensate in these examples experiences additional expansion due to the repulsive s -wave scattering interactions. Such an expansion is accompanied by a faster reduction of the molecular peak density [see Fig. 12(a)] compared to the cases with no molecule-molecule interactions. Indeed, as we see in Fig. 12(a) the molecular peak density for the dashed red and dotted magenta curves drops faster than for the other two curves, yet the atom number growths for the same cases is the slowest in Fig. 11. Thus, the reduction in the molecular density takes place not only because of the conversion to atoms, but also because of the expansion of the molecular condensate. Our estimates show that at $t/t_0 \simeq 3$ the simple expansion alone would reduce the molecular density to 0.95 of the original value, which is a larger effect than the reduction due to conversion to atoms. In terms of an instantaneous effective coupling $\chi \langle \hat{\Psi}_0(x,t) \rangle$ (interpreted at the level of a time-dependent mean field), which is similar to $g(x) = \chi \sqrt{\rho_0(x,0)}$ used previously in the

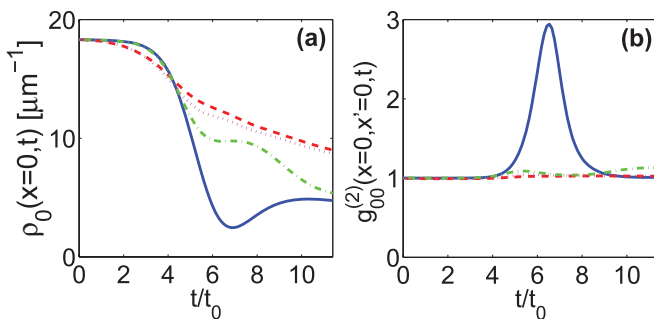


FIG. 12. (Color online) (a) Peak molecular density $\rho_0(0,t)$ as a function of time. The different curves are as in Fig. 11. (b) Molecule-molecule local pair correlation in the center of the molecular cloud $g_{00}^{(2)}(x=0,x'=0,t)$ as a function of time, for the same curves as in (a).

undepleted molecular approximation, the additional reduction in the molecular density means that the instantaneous atom-molecule coupling and therefore the rate of conversion into atoms is reduced more than in the case with no expansion of the molecular condensate. Accordingly, the dashed red and dotted magenta curves in Fig. 11 have the slowest growth in the atom number.

The “bending” of the curves at later times can be explained by the effect of phase diffusion due to the s -wave scattering interactions. The phase diffusion leads to dynamical dephasing of the phase-matching condition for efficient conversion, thus suppressing an exponential amplification in the atom number growth. The characteristic time scale for phase diffusion in the initial stages of dissociation can be estimated via

$$t_d \simeq \frac{2\pi}{|U_{01}^{(1D)} - \frac{1}{2}U_{00}^{(1D)}|\rho_0}, \quad (75)$$

which gives the following results for the three cases shown in Fig. 11: $t_d/t_0 \simeq 4.6$ for the case with $a_{01} \neq 0$, $t_d/t_0 \simeq 9.8$ for the case with $a_{00} \neq 0$, and $t_d/t_0 \simeq 8.7$ for the case with all s -wave scattering interactions present. Here we have ignored the contribution coming from the atomic mean field itself (as the atomic density is initially negligibly small compared to the molecular peak density) and ignored the fact that the mean-field phase shifts are spatially dependent and dynamically changing. With these remarks in mind, we find that our order-of-magnitude estimates of the phase diffusion time are consistent with the numerical results seen in Fig. 11. Moreover, a model simulation of a uniform system with the same s -wave scattering interaction terms as in the relevant three cases of Fig. 11 reproduce the trend that follows from these simple estimates and the order of the curves that experience progressively slower phase diffusion.

In addition to monitoring the dynamics of the molecular peak density, we have analyzed the second-order correlation function $g_{00}^{(2)}(x,x',t)$ for the molecular field in position space in order to understand the deviation of the molecular field from the initial coherent state. In Fig. 12(b) we show the molecule-molecule local pair correlation in the center of the cloud $g_{00}^{(2)}(0,0,t)$ as a function of time for the same examples as in Fig. 12(a). We see that the strongest deviation from the coherent state value of $g_{00}^{(2)}(0,0,t) = 1$ occurs for the case with the strongest depletion, corresponding to the absence of s -wave scattering interactions (solid blue curve). In this case, the minimum in the peak molecular density—occurring approximately at $t/t_0 \sim 6.5$ —is the smallest and is closer to zero, implying that the quantum fluctuations are no longer negligible compared to the mean-field part. As a signature of this, we see a respective peak in the pair correlation function, $g_{00}^{(2)}(0,0,t) \simeq 3$, around the same time. In contrast to this, in cases with s -wave scattering interactions, the molecular depletion is weaker, the peak density is still high enough, and therefore the molecular field remains closer to the initial coherent state in terms of the second-order coherence, with $g_{00}^{(2)}(0,0,t) \simeq 1$.

Finally, in Fig. 13 we plot the back-to-back pair correlation function for the dissociated atoms in momentum space and monitor it as a function of time. The different curves (solid, dashed, dash-dotted, and dotted) are for the

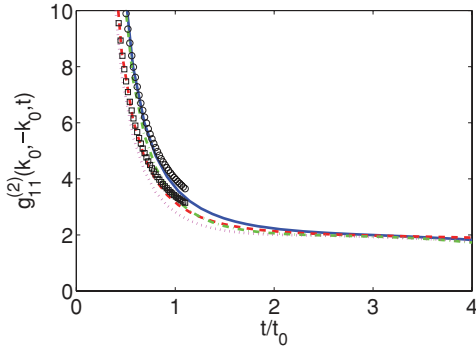


FIG. 13. (Color online) Back-to-back pair correlation for dissociated atoms, $g_{11}^{(2)}(k_0, -k_0, t)$, as a function of time. The different curves (solid blue, dash-dotted green, dashed red, and dotted magenta) are as in Fig. 11. The black squares and circles are the results from short-time analytic solutions given by Eqs. (76) and (77), respectively.

same numerical examples as in Fig. 11, showing that the s -wave scattering interactions—while certainly affecting the quantitative details—have a relatively smaller effect on atom-atom correlation functions at least for dissociation durations up to $t/t_0 \simeq 4$. Moreover, the numerical results for $t/t_0 \lesssim 1$ are in surprisingly good agreement with the short-time analytic results (shown as squares for the case of the initial TF density profile of the molecular BEC and as circles for the initial Gaussian profiles), which in the strict sense were meant to be applicable only for $t/t_0 \ll 1$. The analytic results for the present case of indistinguishable bosons follow from Eq. (22), which for $k' = -k$ reads as $g_{11}^{(2)}(k, -k, t) = 2 + |m(k, -k, t)|^2/[n(k, t)]^2$. Using the asymptotic expressions in 1D given by Eqs. (36) and (37) for the case of the TF parabola, we obtain

$$g_{11}^{(2)}(k, -k, t) \simeq 2 + \frac{9\pi^2}{64\chi^2 t^2 \rho_0}. \quad (76)$$

Similarly, using Eqs. (64) and (65) for the Gaussian density profile, we obtain

$$g_{11}^{(2)}(k, -k, t) \simeq 2 + \frac{2}{\chi^2 t^2 \rho_0}. \quad (77)$$

Both these expressions have inverse square dependence on time t and are shown in Fig. 13 by the curves corresponding to squares and circles.

VII. SUMMARY

We have analyzed the quantum dynamics of dissociation of harmonically trapped Bose-Einstein condensates of molecular dimers in one, two, and three spatial dimensions. More specifically, we have initially examined how the spatial inhomogeneity of the molecular condensate affects the conversion dynamics and the atom-atom correlations in momentum space in the short-time limit. Both fermionic and bosonic statistics of the constituent atom pairs were considered. Using the undepleted molecular-field approximation, we have obtained explicit analytic results for the short-time asymptotic behavior of the pair correlation functions and the relative atom number squeezing.

For a TF parabolic density profile of the molecular BEC, the correlation functions can be expressed in terms of Bessel functions and are determined by the momentum distribution of the source molecular BEC. The precise relationship is different in one, two, and three dimensions. We have compared the results corresponding to the TF density profile with those corresponding to a simple Gaussian and found that the correlation widths relative to the source width are smaller in the TF case. We have also shown that the relative atom number squeezing in a given atom counting volume is determined merely by the characteristic size of the molecular BEC and by a shape-dependent geometric factor and that the squeezing improves as the size of the BEC is increased. The strength of atom-atom correlations for equal but opposite momenta and the relative number squeezing are the strongest in 1D systems, where the mode-mixing is a relatively weaker effect than in higher dimensions.

The analytic and numerical results in the undepleted molecular-field approximation have been compared with exact numerical simulations using the positive- P representation in 1D, as well as with simulations using the truncated Wigner approach, both of which are suitable for treating the molecular-field dynamics and its depletion. The comparison shows that in the absence of any s -wave scattering interactions the undepleted molecular approximation is valid for dissociation durations corresponding to $\sim 10\%$ conversion of molecules into free atoms. We have also examined the role of the s -wave scattering interactions within the truncated Wigner approach and found that the phase diffusion due to these interactions can significantly modify the conversion dynamics in the long time limit. Nevertheless, for dissociation durations corresponding to $\sim 5\%$ conversion, one can still neglect these interactions and use the undepleted molecular approximation. Furthermore, our results indicate that a possible route to extending the validity of the undepleted molecular approximation and minimizing the role of collisional interactions is to operate at larger absolute values of both the atom-molecule coupling χ and the dissociation detuning $|\Delta|$.

Even though 5%–10% conversion efficiencies seem small, nevertheless they can produce mesoscopic ensembles of pair-correlated atoms with interesting quantum statistics and nontrivial many-body correlations if one starts with large-enough molecular condensates, such as containing 10^4 – 10^5 molecules in typical 1D configurations. Accordingly, our simple analytic results in the undepleted molecular approximation provide a useful tool for obtaining qualitative insights and better than “order-of-magnitude” estimates for realistic inhomogeneous systems. For a specific system at hand, these results can be further refined using the positive- P and truncated Wigner methods as demonstrated in the present study.

ACKNOWLEDGMENTS

The authors thank C. M. Savage for useful discussions and acknowledge support by the Australian Research Council through the ARC Centre of Excellence scheme. M.Ö. acknowledges support by IPRS/UQILAS and the Solander Program at UQ.

APPENDIX A: CORRELATION INTEGRALS IN 2D

We first evaluate the integral in the anomalous density $|m_{12}(\mathbf{k}, \mathbf{k}', t)|$ [Eq. (26)], in which we take $\mathbf{k}' = -\mathbf{k} + \mathbf{e}_i \Delta k_i$, so that the integral takes the form

$$|m_{12}(k_x, k'_x, t)| = \frac{t\chi\sqrt{\rho_0}}{(2\pi)^2} \int_{\Lambda} dx dy e^{i(k_x+k'_x)x} \times \left(1 - \frac{x^2}{R_{\text{TF},x}^2} - \frac{y^2}{R_{\text{TF},y}^2}\right)^{1/2}, \quad (\text{A1})$$

where the integration domain Λ is given by $x^2/R_{\text{TF},x}^2 + y^2/R_{\text{TF},y}^2 < 1$. For definiteness, we have chosen the direction i to be the x axis, without the loss of generality. Introducing scaled variables, $x' = x/R_{\text{TF},x}$ and $y' = y/R_{\text{TF},y}$, and transforming to polar coordinates $x' = r \cos \theta$ and $y' = r \sin \theta$, the integral can be rewritten as

$$|m_{12}(k_x, k'_x, t)| = \frac{t\chi\sqrt{\rho_0}R_{\text{TF},x}R_{\text{TF},y}}{(2\pi)^2} \int_0^1 dr r (1-r^2)^{1/2} \times \int_0^{2\pi} d\theta e^{i(k_x+k'_x)R_{\text{TF},x}r \cos \theta}. \quad (\text{A2})$$

Using the integral representation of the zeroth-order Bessel function [73]

$$J_0(z) = \frac{1}{\pi} \int_0^\pi d\theta e^{iz \cos \theta}, \quad (\text{A3})$$

the integral in Eq. (A2) can be brought into the following form:

$$|m_{12}(k_x, k'_x, t)| = \frac{t\chi\sqrt{\rho_0}R_{\text{TF},x}R_{\text{TF},y}}{2\pi} \times \int_0^1 dr r (1-r^2)^{1/2} J_0[(k_x+k'_x)R_{\text{TF},x}r]. \quad (\text{A4})$$

By making a variable change $r = \sin \phi$ and using the integral representation of the Bessel function of general order [73],

$$J_{\rho+\mu+1}(q)2^\rho \Gamma(\rho+1)q^{-\rho-1} = \int_0^{\pi/2} d\phi J_\mu(q \sin \phi) (\sin \phi)^{\mu+1} (\cos \phi)^{2\rho+1}, \quad (\text{A5})$$

with $\text{Re} \rho > -1$ and $\text{Re} \mu > -1$, we finally obtain

$$|m_{12}(k_x, k'_x, t)| \simeq \frac{t\chi\sqrt{\rho_0}R_{\text{TF},x}R_{\text{TF},y}}{2\sqrt{2\pi}} \frac{J_{3/2}[(k_x+k'_x)R_{\text{TF},x}]}{[(k_x+k'_x)R_{\text{TF},x}]^{3/2}}. \quad (\text{A6})$$

If the displacement direction i was along y , we would obtain the same results except $k_x \rightarrow k_y$, by defining the polar coordinates according to $x' = r \sin \theta'$ and $y' = r \cos \theta'$. Thus, by replacing in $|m_{12}(k_x, k'_x, t)|$ the k_x and k'_x components with k_i and k'_i ($i = x, y$), we arrive at the general result of Eq. (41).

To evaluate the integrals in the normal density $n_j(\mathbf{k}, \mathbf{k}', t)$ [Eq. (27)], in which we take $\mathbf{k}' = \mathbf{k} + \mathbf{e}_i \Delta k_i$, and

therefore

$$n_j(k_x, k'_x, t) = \frac{t^2\chi^2\rho_0}{(2\pi)^2} \int_{\Lambda} dx dy e^{i(k_x-k'_x)x} \times \left(1 - \frac{x^2}{R_{\text{TF},x}^2} - \frac{y^2}{R_{\text{TF},y}^2}\right), \quad (\text{A7})$$

we follow the same steps as in evaluating $|m_{12}(k_x, k'_x, t)|$. In polar coordinates, the preceding integral can be brought into the following form:

$$n_j(k_x, k'_x, t) = \frac{t^2\chi^2\rho_0}{(2\pi)^2} \int_0^1 dr r (1-r^2) \int_0^{2\pi} d\theta e^{i(k_x-k'_x)R_{\text{TF},x}r \cos \theta} = \frac{t^2\chi^2\rho_0 R_{\text{TF},x} R_{\text{TF},y}}{2\pi} \int_0^1 dr r (1-r^2) J_0[(k_x-k'_x)R_{\text{TF},x}r]. \quad (\text{A8})$$

Introducing $r = \sin \phi$ and using Eq. (A5), the integration with respect to ϕ gives

$$n_j(k_x, k'_x, t) \simeq \frac{t^2\chi^2\rho_0 R_{\text{TF},x} R_{\text{TF},y}}{\pi} \frac{J_2[(k_x-k'_x)R_{\text{TF},x}]}{[(k_x-k'_x)R_{\text{TF},x}]^2}. \quad (\text{A9})$$

The same result, except $k_x \rightarrow k_y$, can be obtained if the displacement is along y , and we arrive at the general result of Eq. (42).

Finally, the calculation of the integral in

$$n_0(k_i) = \left| \int d^2\mathbf{x} \sqrt{\rho_0(\mathbf{x})} \exp(-ik_i x_i) / (2\pi) \right|^2 \quad (\text{A10})$$

follows the same pattern as in $|m_{12}(k_i, k'_i, t)|$ except that the relevant term is squared, and one obtains Eq. (47).

APPENDIX B: CORRELATION INTEGRALS IN 3D

We first evaluate the 3D integral in the anomalous density $|m_{12}(\mathbf{k}, \mathbf{k}', t)|$ [Eq. (26)], in which we take $\mathbf{k}' = -\mathbf{k} + \mathbf{e}_i \Delta k_i$. For definiteness, we choose the direction i to be along z , so that the integral takes the form

$$|m_{12}(k_z, k'_z, t)| = \frac{t\chi\sqrt{\rho_0}}{(2\pi)^3} \int_{\Lambda} dx dy dz e^{i(k_z+k'_z)z} \times \left(1 - \frac{x^2}{R_{\text{TF},x}^2} - \frac{y^2}{R_{\text{TF},y}^2} - \frac{z^2}{R_{\text{TF},z}^2}\right)^{1/2}, \quad (\text{B1})$$

where the integration domain Λ is defined by $x^2/R_{\text{TF},x}^2 + y^2/R_{\text{TF},y}^2 + z^2/R_{\text{TF},z}^2 < 1$. Introducing scaled variables, $x' = x/R_{\text{TF},x}$, $y' = y/R_{\text{TF},y}$, and $z' = z/R_{\text{TF},z}$ and transforming to spherical coordinates $x' = r \sin \theta \cos \varphi$, $y' = r \sin \theta \sin \varphi$, and $z' = r \cos \theta$, the integral can be rewritten as

$$|m_{12}(k_z, k'_z, t)| = \frac{t\chi\sqrt{\rho_0}R_{\text{TF},x}R_{\text{TF},y}R_{\text{TF},z}}{(2\pi)^3} \int_0^{2\pi} d\varphi \int_0^1 dr r^2 (1-r^2)^{1/2} \times \int_0^\pi d\theta \sin \theta e^{i(k_z+k'_z)R_{\text{TF},z}r \cos \theta}. \quad (\text{B2})$$

The integral with respect to φ is trivial, while the integral with respect to θ is taken using [73]

$$J_\nu(q)\Gamma(\nu + 1/2) = \pi^{-1/2}(q/2)^\nu \int_0^\pi d\theta (\sin\theta)^{2\nu} e^{iq \cos\theta}, \quad (\text{B3})$$

where $\text{Re}\nu > -1/2$. This gives

$$|m_{12}(k_z, k'_z, t)| = \frac{t\chi\sqrt{\rho_0}R_{\text{TF},x}R_{\text{TF},y}R_{\text{TF},z}}{(2\pi)^{3/2}[(k_z + k'_z)R_{\text{TF},z}]^{1/2}} \times \int_0^1 dr r^{3/2}(1-r^2)^{1/2} \times J_{1/2}[(k_z + k'_z)R_{\text{TF},z}r], \quad (\text{B4})$$

which in turn takes the form of Eq. (A5) if we introduce $r = \sin\phi$. Accordingly, we obtain

$$|m_{12}(k_z, k'_z, t)| = \frac{t\chi\sqrt{\rho_0}R_{\text{TF},x}R_{\text{TF},y}R_{\text{TF},z}}{4\pi} \frac{J_2[(k_z + k'_z)R_{\text{TF},z}]}{[(k_z + k'_z)R_{\text{TF},z}]^2}. \quad (\text{B5})$$

For displacements along $i = x$ or $i = y$ directions, one can obtain the same result except that k_z is replaced by k_i by an appropriate rotation of the spherical coordinate system, so that the final result for $|m_{12}(k_i, k'_i, t)|$ takes the form of Eq. (52).

To evaluate the integral in the normal density $n_j(\mathbf{k}, \mathbf{k}', t)$ [Eq. (27)], in which $\mathbf{k}' = \mathbf{k} + \mathbf{e}_i \Delta k_i$, we follow the same steps

as for evaluating $m_{12}(\mathbf{k}, \mathbf{k}', t)$. In spherical coordinates, the integral takes the following form:

$$n_j(k_z, k'_z, t) = \frac{t^2\chi^2\rho_0R_{\text{TF},x}R_{\text{TF},y}R_{\text{TF},z}}{(2\pi)^3} \int_0^{2\pi} d\varphi \times \int_0^1 dr r^2(1-r^2) \int_0^\pi d\theta \sin\theta e^{i(k_z - k'_z)R_{\text{TF},z}r \cos\theta} = \frac{t^2\chi^2\rho_0R_{\text{TF},x}R_{\text{TF},y}R_{\text{TF},z}}{(2\pi)^{3/2}[(k_z - k'_z)R_{\text{TF},z}]^{1/2}} \times \int_0^1 dr r^{3/2}(1-r^2) J_{1/2}[(k_z - k'_z)R_{\text{TF},z}r], \quad (\text{B6})$$

where we have used Eq. (B3). Introducing $r = \sin\phi$ and using Eq. (A5), we obtain

$$n_j(k_z, k'_z, t) = \frac{t^2\chi^2\rho_0R_{\text{TF},x}R_{\text{TF},y}R_{\text{TF},z}}{\pi\sqrt{2\pi}} \frac{J_{5/2}[(k_z - k'_z)R_{\text{TF},z}]}{[(k_z - k'_z)R_{\text{TF},z}]^{5/2}}. \quad (\text{B7})$$

Generalizing this to the arbitrary displacement direction i leads to the final result of Eq. (53).

Finally, the calculation of the integral in

$$n_0(k_i) = \left| \int d^3\mathbf{x} \sqrt{\rho_0(\mathbf{x})} \exp(-ik_i x_i) / (2\pi)^{3/2} \right|^2 \quad (\text{B8})$$

follows the same pattern as the evaluation of $|m_{12}(k_i, k'_i, t)|$, and we obtain Eq. (58).

-
- [1] A. Aspect, P. Grangier, and G. Roger, *Phys. Rev. Lett.* **47**, 460 (1981).
- [2] D. C. Burnham and D. L. Weinberg, *Phys. Rev. Lett.* **25**, 84 (1970).
- [3] C. K. Hong, Z. Y. Ou, and L. Mandel, *Phys. Rev. Lett.* **59**, 2044 (1987).
- [4] A. Aspect, P. Grangier, and G. Roger, *Phys. Rev. Lett.* **49**, 91 (1982); A. Aspect, J. Dalibard, and G. Roger, *ibid.* **49**, 1804 (1982).
- [5] W. Perrie, A. J. Duncan, H. J. Beyer, and H. Kleinpoppen, *Phys. Rev. Lett.* **54**, 1790 (1985).
- [6] Z. Y. Ou and L. Mandel, *Phys. Rev. Lett.* **61**, 50 (1988).
- [7] Y. H. Shih and C. O. Alley, *Phys. Rev. Lett.* **61**, 2921 (1988).
- [8] D. Bohm, *Quantum Theory* (Prentice-Hall, Englewood Cliffs, NJ, 1951).
- [9] A. Einstein, B. Podolsky, and N. Rosen, *Phys. Rev.* **47**, 777 (1935).
- [10] Z. Y. Ou, S. F. Pereira, H. J. Kimble, and K. C. Peng, *Phys. Rev. Lett.* **68**, 3663 (1992).
- [11] T. Mukaiyama, J. R. Abo-Shaer, K. Xu, J. K. Chin, and W. Ketterle, *Phys. Rev. Lett.* **92**, 180402 (2004).
- [12] S. Dürr, T. Volz, and G. Rempe, *Phys. Rev. A* **70**, 031601(R) (2004).
- [13] M. Greiner, C. A. Regal, J. T. Stewart, and D. S. Jin, *Phys. Rev. Lett.* **94**, 110401 (2005).
- [14] S. T. Thompson, E. Hodby, and C. E. Wieman, *Phys. Rev. Lett.* **94**, 020401 (2005).
- [15] S. Knoop, M. Mark, F. Ferlaino, J. G. Danzl, T. Kraemer, H.-C. Nägerl, and R. Grimm, *Phys. Rev. Lett.* **100**, 083002 (2008).
- [16] U. V. Poulsen and K. Mølmer, *Phys. Rev. A* **63**, 023604 (2001).
- [17] K. V. Kheruntsyan and P. D. Drummond, *Phys. Rev. A* **66**, 031602(R) (2002); K. V. Kheruntsyan, *ibid.* **71**, 053609 (2005).
- [18] A. Vardi and M. G. Moore, *Phys. Rev. Lett.* **89**, 090403 (2002).
- [19] V. A. Yurovsky and A. Ben-Reuven, *Phys. Rev. A* **67**, 043611 (2003).
- [20] T. Opatrný and G. Kurizki, *Phys. Rev. Lett.* **86**, 3180 (2001).
- [21] K. V. Kheruntsyan, M. K. Olsen, and P. D. Drummond, *Phys. Rev. Lett.* **95**, 150405 (2005).
- [22] B. Zhao, Z.-B. Chen, J.-W. Pan, J. Schmiedmayer, A. Recati, G. E. Astrakharchik, and T. Calarco, *Phys. Rev. A* **75**, 042312 (2007).
- [23] E. S. Fry, T. Walther, and S. Li, *Phys. Rev. A* **52**, 4381 (1995).
- [24] C. Gneiting and K. Hornberger, *Phys. Rev. Lett.* **101**, 260503 (2008).
- [25] J. Deiglmayr, A. Grochola, M. Repp, K. Mörtilbauer, C. Glöck, J. Lange, O. Dulieu, R. Wester, and M. Weidemüller, *Phys. Rev. Lett.* **101**, 133004 (2008).
- [26] F. Lang, K. Winkler, C. Strauss, R. Grimm, and J. Hecker Denschlag, *Phys. Rev. Lett.* **101**, 133005 (2008).
- [27] K.-K. Ni, S. Ospelkaus, M. H. G. de Miranda, A. Pe'er, B. Neyenhuis, J. J. Zirbel, S. Kotochigova, P. S. Julienne, D. S. Jin, and J. Ye, *Science* **322**, 231 (2008).
- [28] M. Yasuda and F. Shimizu, *Phys. Rev. Lett.* **77**, 3090 (1996).

- [29] S. Fölling, F. Gerbier, A. Widera, O. Mandel, T. Gericke, and I. Bloch, *Nature (London)* **434**, 481 (2005); T. Rom, T. Best, D. van Oosten, U. Schneider, S. Fölling, B. Paredes, and I. Bloch, *ibid.* **444**, 733 (2006).
- [30] C.-S. Chuu, F. Schreck, T. P. Meyrath, J. L. Hanssen, G. N. Price, and M. G. Raizen, *Phys. Rev. Lett.* **95**, 260403 (2005).
- [31] A. Öttl, S. Ritter, M. Köhl, and T. Esslinger, *Phys. Rev. Lett.* **95**, 090404 (2005).
- [32] M. Schellekens, R. Hoppeler, A. Perrin, J. V. Gomes, D. Boiron, A. Aspect, and C. I. Westbrook, *Science* **310**, 648 (2005); T. Jeltes *et al.*, *Nature (London)* **445**, 402 (2007).
- [33] J. Esteve, J.-B. Trebbia, T. Schumm, A. Aspect, C. I. Westbrook, and I. Bouchoule, *Phys. Rev. Lett.* **96**, 130403 (2006).
- [34] A. Perrin, H. Chang, V. Krachmalnicoff, M. Schellekens, D. Boiron, A. Aspect, and C. I. Westbrook, *Phys. Rev. Lett.* **99**, 150405 (2007).
- [35] A. J. Ferris, M. K. Olsen, E. G. Cavalcanti, and M. J. Davis, *Phys. Rev. A* **78**, 060104(R) (2008).
- [36] K. V. Kheruntsyan, *Phys. Rev. Lett.* **96**, 110401 (2006).
- [37] M. W. Jack and H. Pu, *Phys. Rev. A* **72**, 063625 (2005).
- [38] D. F. Walls and G. J. Milburn, *Quantum Optics* (Springer, Berlin, 2008), 2nd ed.
- [39] C. M. Savage, P. E. Schwenn, and K. V. Kheruntsyan, *Phys. Rev. A* **74**, 033620 (2006).
- [40] C. M. Savage and K. V. Kheruntsyan, *Phys. Rev. Lett.* **99**, 220404 (2007).
- [41] J. F. Corney and P. D. Drummond, *Phys. Rev. Lett.* **93**, 260401 (2004).
- [42] S. L. W. Midgley, S. Wüster, M. K. Olsen, M. J. Davis, and K. V. Kheruntsyan, *Phys. Rev. A* **79**, 053632 (2009).
- [43] M. Ögren, K. V. Kheruntsyan, and J. F. Corney, e-print arXiv:0910.4440v2.
- [44] M. J. Davis, S. J. Thwaite, M. K. Olsen, and K. V. Kheruntsyan, *Phys. Rev. A* **77**, 023617 (2008).
- [45] M. Haque and H. T. C. Stoof, *Phys. Rev. A* **71**, 063603 (2005).
- [46] M. Ögren and K. V. Kheruntsyan, *Phys. Rev. A* **79**, 021606(R) (2009).
- [47] A. Perrin, C. M. Savage, D. Boiron, V. Krachmalnicoff, C. I. Westbrook, and K. V. Kheruntsyan, *New J. Phys.* **10**, 045021 (2008).
- [48] M. Ögren and K. V. Kheruntsyan, *Phys. Rev. A* **78**, 011602(R) (2008).
- [49] M. Ögren, C. M. Savage, and K. V. Kheruntsyan, *Phys. Rev. A* **79**, 043624 (2009).
- [50] I. Tikhonenkov and A. Vardi, *Phys. Rev. Lett.* **98**, 080403 (2007); *J. Phys. B* **40**, S299 (2007).
- [51] S. Brouard and J. Plata, *Phys. Rev. A* **72**, 023620 (2005); J. Plata, *ibid.* **74**, 013603 (2006).
- [52] T. Miyakawa and P. Meystre, *Phys. Rev. A* **74**, 043615 (2006).
- [53] U. V. Poulsen and K. Mølmer, *Phys. Rev. A* **76**, 013614 (2007).
- [54] I. Tikhonenkov, E. Pazy, Y. B. Band, and A. Vardi, *Phys. Rev. A* **77**, 063624 (2008).
- [55] I. Tikhonenkov and A. Vardi, *Phys. Rev. A* **80**, 051604(R) (2009).
- [56] T. Köhler, E. Tiesinga, and P. S. Julienne, *Phys. Rev. Lett.* **94**, 020402 (2005).
- [57] S. Dürr, T. Volz, N. Syassen, G. Rempe, E. van Kempen, S. Kokkelmans, B. Verhaar, and H. Friedrich, *Phys. Rev. A* **72**, 052707 (2005).
- [58] E. Braaten and D. Zhang, *Phys. Rev. A* **73**, 042707 (2006).
- [59] T. M. Hanna, K. Góral, E. Witkowska, and T. Köhler, *Phys. Rev. A* **74**, 023618 (2006).
- [60] P. D. Drummond, K. V. Kheruntsyan, and H. He, *J. Opt. B* **1**, 387 (1999); K. V. Kheruntsyan and P. D. Drummond, *Phys. Rev. A* **61**, 063816 (2000).
- [61] P. D. Drummond, K. V. Kheruntsyan, and H. He, *Phys. Rev. Lett.* **81**, 3055 (1998); K. V. Kheruntsyan and P. D. Drummond, *Phys. Rev. A* **58**, 2676(R) (1998).
- [62] D. J. Heinzen, R. H. Wynar, P. D. Drummond, and K. V. Kheruntsyan, *Phys. Rev. Lett.* **84**, 5029 (2000).
- [63] E. Timmermans, P. Tommasini, R. Côté, M. Hussein, and A. Kerman, *Phys. Rev. Lett.* **83**, 2691 (1999); E. Timmermans, P. Tommasini, M. Hussein, and A. Kerman, *Phys. Rep.* **315**, 199 (1999).
- [64] P. D. Drummond and K. V. Kheruntsyan, *Phys. Rev. A* **70**, 033609 (2004).
- [65] J. Javanainen and M. Mackie, *Phys. Rev. A* **59**, R3186 (1999).
- [66] M. Holland, J. Park, and R. Walser, *Phys. Rev. Lett.* **86**, 1915 (2001); S. J. J. M. F. Kokkelmans and M. J. Holland, *ibid.* **89**, 180401 (2002).
- [67] R. A. Duine and H. T. C. Stoof, *Phys. Rep.* **396**, 115 (2004).
- [68] T. Köhler, K. Góral, and P. S. Julienne, *Rev. Mod. Phys.* **78**, 1311 (2006).
- [69] In realistic experimental systems that are designed to detect atom-atom correlations in position space (rather than in momentum space) after time-of-flight expansion, further considerations arise which are due to the initial position uncertainty of the molecules and the detector resolution, as discussed in Ref. [40].
- [70] As a model system for physical parameters in the case of fermionic atoms, we consider a 1D BEC of bosonic $^{40}\text{K}_2$ dimers ($m_0 = 2m = 1.33 \times 10^{-25}$ kg) having the peak 3D density $\rho_0^{(3D)} = 10^{20} \text{ m}^{-3}$ in the trap center. Choosing the transverse trap frequency $\omega_{\perp}/2\pi = 1$ kHz gives the peak 1D density $\rho_0 \equiv \rho_0^{(1D)} = 4\pi l_{\perp}^2 \rho_0^{(3D)} = 4 \times 10^7 \text{ m}^{-1}$, where $l_{\perp} = \sqrt{\hbar/m_0\omega_{\perp}} \simeq 0.355 \text{ }\mu\text{m}$ is the transverse harmonic oscillator length. Choosing next the molecule-molecule s -wave scattering length (in 3D) to be $a_{00} = 3$ nm as an example, one can calculate the 1D coupling strength for the molecule-molecule interaction, $U_{00}^{(1D)} \simeq 2\omega_{\perp}a$. In the regime of weak interactions [$\gamma \ll 1$, where $\gamma = m_0 U_{00}^{(1D)} / (\hbar^2 \rho_0^{(1D)})$], the TF radius of the molecular BEC in the longitudinal direction is given by $R_{\text{TF}} = \sqrt{2\mu/m_0\omega_x^2}$, where $\mu = \hbar U_{00}^{(1D)} \rho_0^{(1D)}$ is the chemical potential and ω_x is the longitudinal trap frequency. In the case of distinguishable bosonic atoms, we assume the same parameters—as a hypothetical example—to make the comparison with the fermionic case directly comparable and dependent only on the quantum statistics.
- [71] R. J. Glauber, *Phys. Rev.* **130**, 2529 (1963); M. Naraschewski and R. J. Glauber, *Phys. Rev. A* **59**, 4595 (1999).
- [72] R. Hanbury Brown and R. Q. Twiss, *Nature (London)* **177**, 27 (1956).
- [73] A. Erdelyi, W. Magnus, F. Oberhettinger, and F. G. Tricomi, *Higher Transcendental Functions* (McGraw-Hill, New York, 1953), Vol. 2.
- [74] P. D. Drummond and C. W. Gardiner, *J. Phys. A* **13**, 2353 (1980); P. D. Drummond and S. J. Carter, *J. Opt. Soc. Am. B* **4**, 1565 (1987).
- [75] M. J. Steel, M. K. Olsen, L. I. Plimak, P. D. Drummond, S. M. Tan, M. J. Collett, D. F. Walls, and R. Graham, *Phys. Rev. A* **58**, 4824 (1998).

- [76] A. Sinatra, C. Lobo, and Y. Castin, *Phys. Rev. Lett.* **87**, 210404 (2001).
- [77] P. Deuar and P. D. Drummond, *Phys. Rev. Lett.* **98**, 120402 (2007).
- [78] V. Krachmalnicoff *et al.*, *Phys. Rev. Lett.* **104**, 150402 (2010).
- [79] A. Gilchrist, C. W. Gardiner, and P. D. Drummond, *Phys. Rev. A* **55**, 3014 (1997).
- [80] P. Deuar and P. D. Drummond, *J. Phys. A* **39**, 2723 (2006).
- [81] For the BEC of $^{87}\text{Rb}_2$ dimers (with $m_1 = 1.44 \times 10^{-25}$ kg and $m_0 = 2m_1$) we consider a 3D density $\rho_0^{(3D)} = 1.3 \times 10^{18}$ m $^{-3}$ in the trap center. Choosing the transverse trap frequency $\omega_\perp/2\pi = 54$ Hz gives the peak 1D density $\rho_0 \equiv \rho_0^{(1D)} = 4\pi l_\perp^2 \rho_0^{(3D)} \simeq 1.8 \times 10^7$ m $^{-1}$, where $l_\perp = \sqrt{\hbar/m_0\omega_\perp} \simeq 1.0$ μm is the transverse harmonic oscillator length for the molecules. With all 3D s -wave scattering lengths set to $a_{ij} = 3$ nm, the

1D coupling strengths are $U_{ii}^{(1D)} = 2\omega_\perp a_{ii} \simeq 2.04 \times 10^{-6}$ m s $^{-1}$ and $U_{01} = 3/\sqrt{2}\omega_\perp a_{01} \simeq 2.16 \times 10^{-6}$ ms $^{-1}$. We use a bare detuning $\Delta = -259$ s $^{-1}$ and a 1D atom-molecule coupling $\chi = 6.7 \times 10^{-3}$ m $^{1/2}$ s $^{-1}$, resulting in the characteristic time scale $t_0 = 1/\chi\sqrt{\rho_0} \simeq 0.035$ s. For the initial density profiles in the examples of Fig. 11 with $a_{00} \neq 0$, we use a numerically determined (near-parabolic) ground-state solution of the GP equation for the molecular BEC in a longitudinal harmonic trap with frequency $\omega_x/2\pi = 1/2$ Hz ($\omega_x \ll \omega_\perp$) and the same peak density ρ_0 as previously. In the TF limit, the respective TF radius is given by $R_{\text{TF}} = \sqrt{4\hbar\omega_\perp a_{00}\rho_0/m_0\omega_x^2} \simeq 53$ μm , and the corresponding initial total number of molecules is $N_0(0) = 1.28 \times 10^3$. For cases with a Gaussian initial density profile, we use $\rho_0(x) = \rho_0 \exp(-x^2/2S_x^2)$ with $S_x \simeq 35$ μm .